A unified state diagram for the yielding transition of soft colloids

Stefano Aime, Domenico Truzzolillo, David Pine, Laurence Ramos, Luca Cipelletti

A unified state diagram for the yielding transition of soft colloids

Stefano Aime*,[1,2] Domenico Truzzolillo,[1] David J. Pine,[3] Laurence Ramos,[1] and Luca Cipelletti*[1,4]

[1] *Laboratoire Charles Coulomb (L2C), Université Montpellier, CNRS, Montpellier, France*

[2] *Present address: ESPCI, Paris, France**

[3] *New York University*

[4] *Institut Universitaire de France*†

(Dated: December 20, 2022)

Abstract

Concentrated colloidal suspensions and emulsions are amorphous soft solids, widespread in technological and industrial applications and studied as model systems in physics and material sciences. They are easily fluidized by applying a mechanical stress, undergoing a yielding transition that still lacks a unified description. Here, we investigate yielding in three classes of repulsive soft solids, using analytical and numerical modelling and experiments probing the microscopic dynamics and mechanical response under oscillatory shear. We find that at the microscopic level yielding consists in a transition between two distinct dynamical states, which we rationalize by proposing a lattice model with dynamical coupling between neighboring sites, leading to a unified state diagram for yielding. Leveraging the analogy with Wan der Waals's phase diagram for real gases, we show that distance from a critical point plays a major role in the emergence of first-order-like *vs* second-order-like features in yielding, thereby reconciling previously contrasting observations on the nature of the transition.

The yielding transition of soft glassy systems is of great relevance both in technological and industrial applications and at a fundamental level [1]. Despite profound differences in their microscopic structural features, yielding occurs with very similar macroscopic features in systems as diverse as colloidal and nanoparticle suspensions [2], emulsions [3–5], star polymers [6] and microgels [7]. This suggests the presence of an underlying general framework, which has been addressed in recent experimental, theoretical and numerical works [8, 9], leading to contrasting results. Measurements of the macroscopic viscoelastic properties suggest that yielding develops progressively as the system is driven far from the linear regime [2, 3, 6, 7, 10]. Various models such as the soft glassy rheology [8], the mode coupling theory [11, 12] and fluidity [13–15] or on-lattice [16] models reproduce the evolution of viscoelastic parameters across yielding. Recent experiments and simulations probing microscopic quantities indicate that yielding is associated with an increase of particle mobility [4, 5, 17–23], suggesting that it may be described as a dynamic transition between a quiescent, solid-like state and a dynamically active, fluid-like state, bearing analogies with equilibrium phase transitions, an approach similar to that used in the past to describe other flow-induced transitions [24]. Note, however, that this description does not take into ac-

* stefano.aime@espci.fr

† luca.cipelletti@umontpellier.fr

count the ultra-slow relaxations that typically occur in soft solids even at rest [25, 26]. These works suggested contrasting scenarios for the yielding transition. Some systems exhibit features typical of a first-order transition, such as a discontinuous jump of the particle mobility [4, 5, 20–22] or of structural symmetries [27], the coexistence of dynamically distinct states [20], and hysteresis [28]. By contrast, in other cases yielding is described as a rather continuous transition [19, 29], with features such as sluggish dynamics [4, 17–19], enhanced fluctuations [4, 30] and growing length scales [19] typically associated with a second-order transition. Thus, the nature of the yielding transition remains elusive: there is a dearth of experiments and modelling addressing the mechanical response and the microscopic dynamics of a class of soft materials sufficiently diverse to allow for a general description of yielding.

Here, we establish a unified view of the yielding transition of repulsive soft colloids by combining experiments probing both microscopic and macroscopic quantities with theoretical modelling and numerical simulations. We investigate samples of three kinds: concentrated suspensions of microgel particles (M) and charged silica nanoparticles (N), and dense emulsions (E) (see Methods for details). All samples exhibit qualitatively similar behavior in oscillatory shear tests at frequency ω and at variable strain amplitude γ_0, as exemplified by Fig. 1a for microgels. For small enough γ_0, G' and G'', the storage and loss moduli, are independent of γ_0, $G' >> G''$ and the stress amplitude σ grows linearly with γ_0, indicative of a predominantly elastic, linear response. As γ_0 is increased, a gradual transition to the nonlinear regime is observed: G' and G'' deviate from their low-γ_0 behavior, with G'' going through a maximum and eventually exceeding G'. Deviations from a purely harmonic response become non-negligible, as shown by the growth of the normalized third harmonic amplitude I_3/I_1 of the stress response. At the largest strain amplitudes, σ grows sublinearly with γ_0 and both moduli decay as power laws: $G' \propto \gamma_0^{-2\nu}$ and $G'' \propto \gamma_0^{-\nu}$, with a sample-dependent exponent ν in the range 0.6-0.75, see Supplementary Table SI1.

The range of strain amplitudes over which rheological quantities signal the transition from solid-like to fluid-like behavior is quite broad, making it difficult to determine the nature of the yielding transition [4, 10]. To gain a deeper insight on yielding, we couple rheometry to measurements of the microscopic dynamics, using dynamic light scattering or differential dynamic microscopy (see Methods). Both methods quantify the dynamics via the intensity correlation function $g_2(\tau) - 1$, which decays from 1 to 0 as microscopic displacements grow

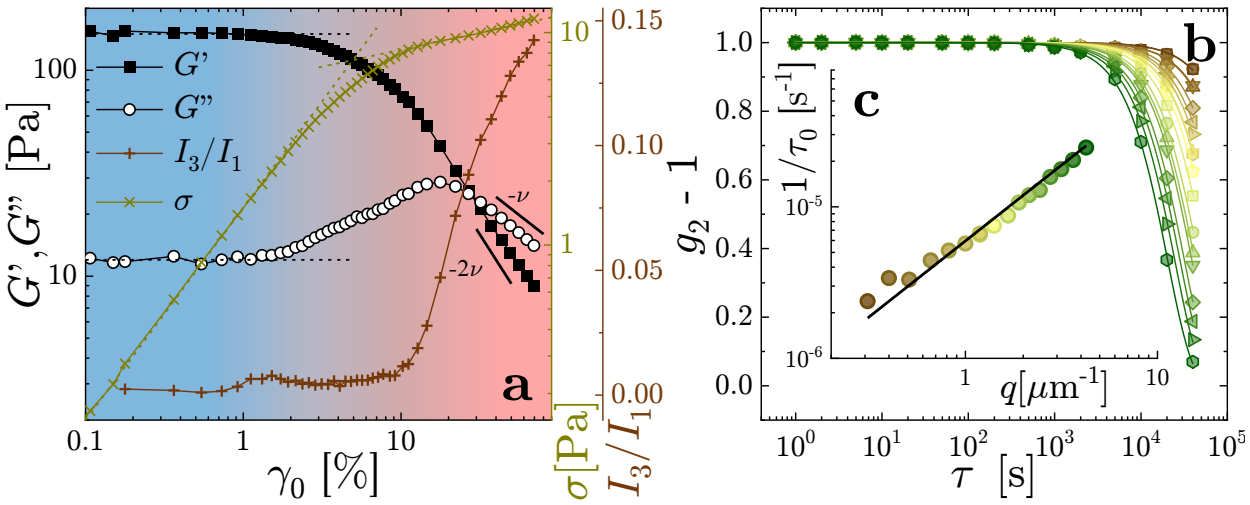

FIG. 1. **Viscoelasticity and spontaneous dynamics of a dense microgel suspension.** a): Oscillatory rheology for a microgel suspension at effective volume fraction $\varphi = 1.5$ (sample M40s). Left axis: first-harmonic storage (G', black squares) and loss (G'', white circles) moduli *vs* strain amplitude γ_0, at fixed $\omega = 0.157$ rad s^{-1}. Right axis: first-harmonic stress amplitude (σ, gold crosses) and normalized third harmonic component of the stress signal (I_3/I_1, brown pluses). Rheological quantities evolve smoothly from solid-like behavior (small γ_0, blue shades) to fluid-like response (red shades). b): Correlation functions measured for the same system at rest, for scattering vectors 0.2 $\mu m^{-1} \leq q \leq 4.5$ μm^{-1}, increasing from brown to green shades. The correlation functions are fitted with compressed exponential functions, with compression exponent $\beta_0 = 1.65 > 1$ (lines). c): Relaxation rate $1/\tau_0$ *vs* scattering vector. Same color code as in b). The line is a fit with slope 1, indicating ballistic dynamics.

beyond a length scale $\pi/q \approx (0.1 - 1)$ μm set by the scattering vector q.

The spontaneous dynamics measured at rest are similar for all samples, and are well described by a slow, compressed exponential relaxation: $g_2^{(s)}(\tau) - 1 = \exp\left[-2\,(\tau/\tau_0)^{\beta_0}\right]$, Fig.1b, with sample-dependent values of the spontaneous relaxation rate $1/\tau_0$ and of the exponent $\beta_0 > 1$, see Supplementary Table SI1. These dynamics are ballistic, as indicated, for the microgels, by the linear dependence of $1/\tau_0$ with q, Fig.1c. Similar spontaneous dynamics have been reported for many other jammed or glassy soft samples at rest, and are attributed to the slow relaxation of quenched internal stresses [25]. To investigate the microscopic dynamics under deformation, we apply an oscillatory shear with angular frequency ω and measure $g_2 - 1$ stroboscopically, for τ values a multiple of the oscillation period $2\pi/\omega$.

The dynamics probed by this echo protocol [31] are only sensitive to irreversible rearrangements, either spontaneous or induced by shear. Figures 2a-c reveal striking similarities of the overall behavior of the correlation functions across all samples. Under small strain amplitudes, the dynamics are independent of γ_0, while they increasingly accelerate with growing strain at larger γ_0. Concomitantly, the shape of $g_2 - 1$ evolves from a steep compressed exponential decay at low γ_0 to a stretched shape at large γ_0. Data at all strain amplitudes are very well fitted by the following expression:

$$g_2(\tau) - 1 = \left\{ \chi \exp\left[-\left(\Gamma_s \omega \tau\right)^{\beta_s} \right] + (1-\chi) \exp\left[-\left(\Gamma_f \omega \tau\right)^{\beta_f} \right] \right\}^2 , \quad (1)$$

where β_f and β_s are (sample-dependent) constants, whereas χ, Γ_s and Γ_f vary with γ_0. The dimensionless relaxation rates for the slow and fast relaxation modes, normalized by the oscillation frequency ω, are designated by Γ_s and Γ_f, respectively.

Figures 2d-f show the strain dependence of the normalized relaxation rates, $\Gamma_{s,f}$, and of the slow mode amplitude χ, obtained by fitting Eq. 1 to the correlation functions of Figs. 2a-c. Three regimes can be distinguished. For small enough strain amplitudes, $g_2 - 1$ relaxes through a single, slow compressed exponential mode ($\chi = 1$), with a stretching exponent $\beta_s \geq 1$ (see Supplementary Table SI1) and a strain-independent relaxation rate Γ_s close to that at rest, $1/\omega\tau_0$. For the microgels, oscillatory tests at $\omega = 0.157$ rad s^{-1} and $\omega = 3.14$ rad s^{-1} indicate no dependence of the slow mode with ω (in physical units), further confirming that the dynamics observed in this regime are unaffected by shear and simply correspond to the sample spontaneous relaxation. As γ_0 exceeds a threshold value, correlation functions become strain-dependent. A second, faster mode, characterized by a stretched exponential relaxation, adds to the spontaneous relaxation mode, whose relative amplitude χ rapidly decays from 1 to 0 with increasing γ_0. Finally, for sufficiently large γ_0, $\chi \approx 0$: the correlation functions are well fitted by a single stretched exponential relaxation, with Γ_f increasing as γ_0^n, with a sample-dependent exponent $1 < n < 8$ (red symbols in Figs 2d-f). In this regime, we check for microgels that the fast relaxation rate, in physical units, is proportional to ω, as expected in the case of dynamics fully dominated by rearrangements induced by strain oscillations. Moreover, we find that for the microgels and emulsions Γ_f scales as q^2 (see Supplementary Figs. SI8-SI9), the hallmark of diffusive motion, as also reported recently in simulations [21] and in experiments on other kinds of microgels under large shear strain [23]. This shear-induced diffusive behavior at large γ_0 is

analogous to the dynamics of *equilibrated* dense colloidal suspensions at rest [32, 33], and contrasts with the ballistic behavior at small strain or at rest. Our experiments thus show that at the microscopic level yielding corresponds to a transition between ultraslow, ballistic relaxations at small γ_0 (unaccounted for in previous works) and fast, diffusive relaxations beyond yielding. In analogy to the recently reported abrupt change of microscopic quantities such as the particle mean squared displacement or diffusivity [4, 21, 23], the amount of irreversible rearrangements [5, 17, 20], and the size of avalanches [22], the correlation functions measured in our experiments exhibit a marked change in a narrow interval of γ_0, indicative of a transition sharper than for rheological quantities, compare the stars and the vertical lines in Figs. 2d-f.

To rationalize these findings, we introduce a simple model. The sample is coarse-grained on a lattice; each lattice site is attributed a relaxation rate Γ_i that depends on both the spontaneous relaxation at rest $1/\omega\tau_0$ and shear-induced rearrangements $\Gamma_{sh,i}$:

$$\Gamma_i = 1/\omega\tau_0 + \Gamma_{sh,i} \tag{2a}$$

$$\Gamma_{sh,i} = \frac{K}{\gamma_0^{-n} + N^{-1}\sum_j \frac{\alpha_{ij}}{\Gamma_i\Gamma_j}}\,, \tag{2b}$$

where K is a constant whose physical meaning will be discussed later, and where the sum in the r.h.s. of Eq. 2b runs over the N nearest neighbors of site i, with $\alpha_{i,j}$ coupling constants between the dynamics of sites i and j. Equation 2a states that the overall relaxation rate is the sum of two independent contributions: $1/\omega\tau_0$, the spontaneous relaxation rate, and $\Gamma_{sh,i}(\gamma_0)$, the site- and strain amplitude-dependent rate of the additional relaxation induced by shear. A similar additive rule has been invoked in mode coupling-based models [34–36], which postulated $\Gamma_{sh,i} \propto \gamma_0^n$. However, this form of the shear-induced relaxation rate yields a smooth growth of Γ_i with γ_0, rather than a well-defined transition. Instead, we propose in Eq. 2b an alternative ansatz for the shear-induced relaxation rate. It is the simplest expression that accounts for the following physical ingredients: i) $\Gamma_{sh,i}$ should vanish for small strain amplitudes, implying $\Gamma_i \approx 1/\omega\tau_0$ in the $\gamma_0 \to 0$ limit; ii) in the opposite limit of large γ_0, the dynamics should be dominated by the externally imposed shear, implying $\Gamma_i \to K\gamma_0^n$, as measured in our experiments for the fast mode; iii) in the intermediate regime, the shear-induced dynamics should be ruled not only by the external drive, but also by the interactions between neighboring sites, which we expect to slow down the system relaxation, as modelled by the sum term in the r.h.s. of Eq. 2b. The latter is chosen in the spirit

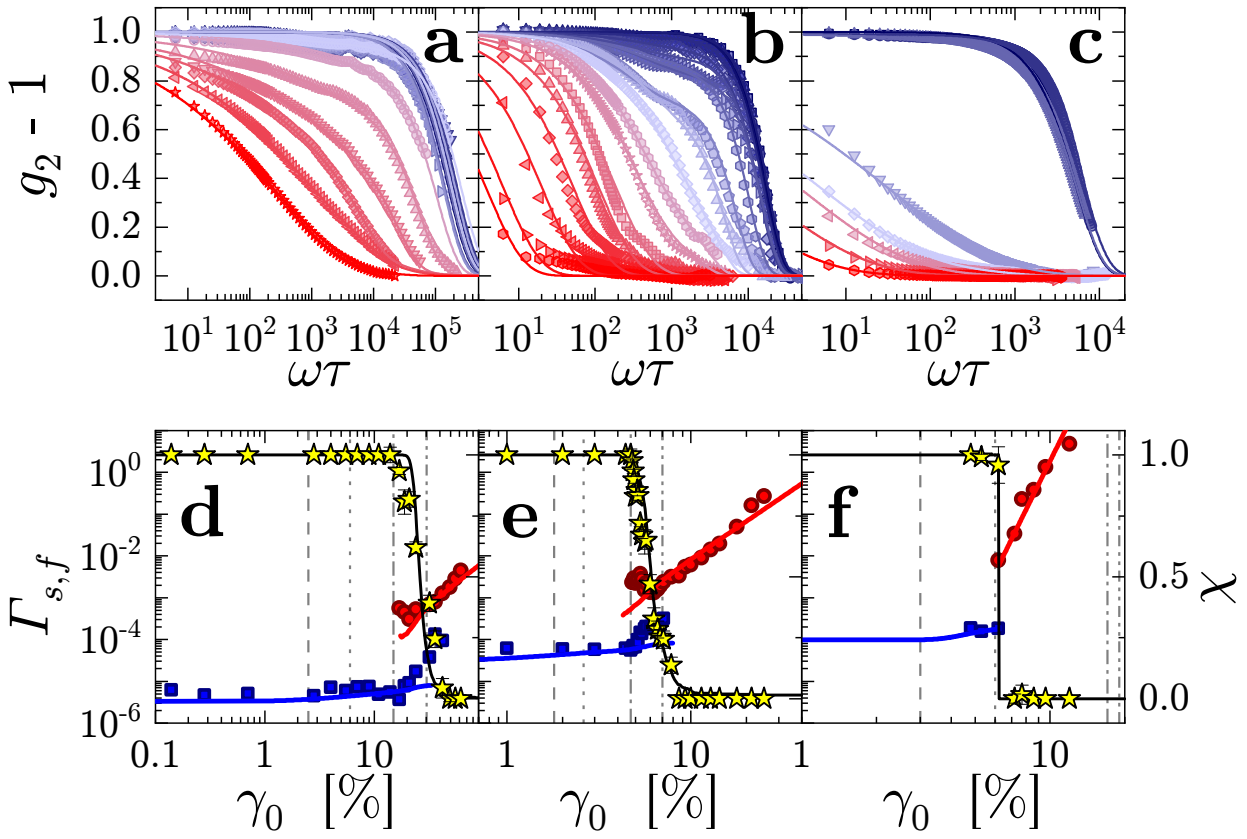

FIG. 2. **Yielding of soft solids as a dynamic transition**. a)-c): Intensity correlation functions under oscillatory shear, for concentrated microgels (a, M2s), nanoparticles (b, N45%), and emulsions (c, E74%), plotted *vs* the normalized time delay $\omega\tau$, with $2\pi/\omega$ the period of the oscillations. $\omega = \pi$ rad/s (resp., 2π rad/s) for samples M2s and N45% (resp., E74%). The strain amplitude γ_0 increases from blue to red shades, spanning the rheological yielding transition (see Methods for sample details and Supplementary Table SI1 for the probed deformation ranges). Symbols: experimental data. Lines: fits using Eq. 1. The compressed exponent β_s of the slow mode is 1.3, 1.9, 1.4 for microgels, nanoparticles, and emulsions, respectively. The stretching exponent β_f of the fast mode is a fit parameter shared between all data for a given sample, yielding $\beta_f = 0.4$, 0.9, and 0.3 for M2s, N45% and E74%, respectively. The fitting parameters for the same samples are shown in d)-f). Left axes: γ_0 dependence of the normalized rates Γ_s (slow mode, blue squares) and Γ_f (fast mode, red circles). Right axes: relative amplitude χ of the slow mode (stars). Lines: numerical results of the general model for the yielding transition discussed in the text, see Supplementary Table SI2 for details on the parameter values. In d)-f), the vertical lines indicate, from left to right, the onset of the increase of G", the onset of deviations from linearity of $\sigma(\gamma_0)$, the maximum of G", the crossover between G' and G".

of dynamic facilitation models for the spontaneous relaxation of glassy systems [37], where sites with a higher-than-average relaxation rate facilitate the relaxation of neighboring sites.

We start by considering the mean-field version of the model, where the coupling constants and thus the relaxation rates are taken to be identical for all sites, $\alpha_{ij} \equiv \alpha$ and $\Gamma_i \equiv \Gamma$. The mean field model can be solved analytically by recasting Eqs. 2 as

$$\left(\Gamma - \frac{1}{\omega\tau_0}\right)\left(\gamma_0^{-n} + \frac{\alpha}{\Gamma^2}\right) = K\,, \tag{3}$$

with α an average coupling constant. This equation is formally identical to the Van der Waals (VdW) equation of state ruling the vapor-liquid transition of real gases, with pressure p volume V and temperature T in the VdW's equation replaced by γ_0^{-n}, Γ, and K, respectively. The spontaneous non-dimensional rate $1/\omega\tau_0$ and the coupling constant α play the role of the molecular volume and molecular interaction parameter in VdW's law, respectively.

In experiments, the strain amplitude is the control parameter, typically plotted on the x axis. In Fig. 3a, we rather choose Γ as the abscissa, to emphasize the analogy of 'iso-K' solutions of Eq. 3 with VdW isotherms in a pV diagram. We find that in the mean field model K plays a key role in differentiating samples that exhibit a yield transition from samples that are predominantly fluid-like at all γ_0, as illustrated by the three curves of Fig. 3a. For K larger than a critical value K_c, solid line in Fig. 3a, γ_0^{-n} decreases monotonically with increasing Γ. This corresponds to the smooth growth — with no yielding transition— of the relaxation rate of concentrated yet equilibrated colloidal fluids upon applying a mechanical drive [38] . For $K < K_c$, by contrast, $\gamma_0^{-n}(\Gamma)$ becomes non-monotonic (dashed line in Fig. 3a): within a finite range of strain amplitudes, a unique value of γ_0 is now associated with multiple values of Γ. In a VdW fluid, this feature is associated with the vapor-liquid phase transition: upon compression, the system jumps from the vapor branch to the fluid branch of the isotherm line at a pressure set by the minimization of the free energy and corresponding to Maxwell's equal area rule. In our model, non-monotonic iso-K curves are associated with yielding. Starting from a solid at rest and increasing progressively γ_0, the system descends the *solid-like* (left) branch of the equation of state, corresponding to small and nearly constant Γ. In the representation of Fig. 3a, portions of the equation of state with positive slope are nonphysical, because they correspond to faster relaxation rates attained at lower strain amplitudes. Thus, the system has to jump from the left branch to the right, fluid branch, which constitutes yielding in our model. We find that in the mean field limit

of the model, the jump occurs at the minimum of the iso-K line, from point (1) to point (2) in Fig. 3a. Introducing disorder smears the transition and, in the limit of small disorder, the yield strain is shifted to smaller values, approaching a value set by the equivalent of Maxwell's equal area rule [39] (points (1') and (2')). Finally, the dotted line of Fig. 3a represents the critical iso-K: in analogy to the VdW's critical isotherm, it has an inflection point but no local minimum. Here, it separates systems that are fluid-like at all γ_0 from systems that are solid-like at small enough γ_0.

The mean field model, Eq. 3, describes yielding as a first-order transition between two dynamically distinct states, accounting for both the linear and the fully fluidized regimes. However, it fails to properly capture the gradual onset of the fast-relaxation mode and the regime of intermediate strain amplitudes where both modes coexist. Quenched disorder is known to smear out first-order transitions [40, 41]. To explore the role of disorder in our case, we solve numerically the full model, Eq. 2, using model parameters that fit the microgels data of Fig. 2d (details in Methods). In the presence of disorder, Γ_i varies from site to site: representative probability distributions $\rho(\Gamma_i)$ are reported for three strain amplitudes in Fig. 3b. In agreement with experiments, three different regimes are seen: (1) under small strain amplitudes, $\rho(\Gamma_i)$ is unimodal, peaked around a small value comparable to the relaxation rate at rest; (2) under intermediate strain amplitudes, $\rho(\Gamma_i)$ becomes bimodal as a consequence of the appearance of a second, faster mode characterized by a rate Γ_f, typically well separated from Γ_s and growing with γ_0; (3) under large strain amplitudes, the slow mode vanishes and $\rho(\Gamma_i)$ is again unimodal, but is now sharply peaked around $\Gamma_f \propto \gamma_0^n$.

We associate the bimodal nature of $\rho(\Gamma_i)$ at intermediate γ_0 with the coexistence of slow and fast relaxation modes observed experimentally, which smears the transition with respect to the mean field prediction (compare the dashed line and the distribution of Γ_i indicated by the color shades in Fig. 3a). A spatial map of the local relaxation rates reveals that slow and fast relaxing sites form a coarse structure (Fig. 3c), consistent with the spatial localization of highly mobile regions observed in the single-cycle dynamics of sheared emulsions [4]. The separation between the two modes allows one to extract from $\rho(\Gamma_i)$ two well-defined values of Γ_s and Γ_f, as well as the relative weight χ of the slow mode. A suitable choice of the model parameters K, n, and of a log-normal distribution of α (see Supplementary Table SI2) reproduces the experimental strain dependence of Γ_s, Γ_f and χ (lines in Fig. 2d-f). The good agreement between experimental data and numerical results over up to two decades in

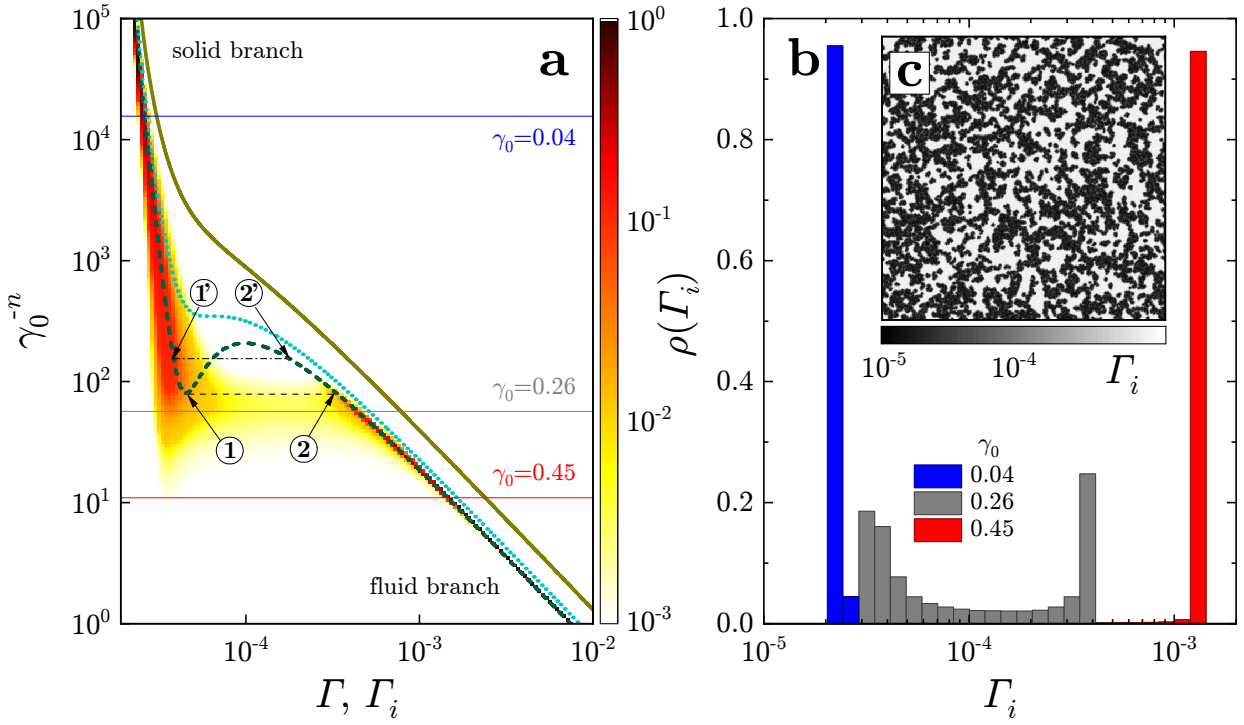

FIG. 3. **Theoretical and numerical modelling of the yielding transition.** a) Lines: mean field model, Eq. 3, for three K values: $K = 4\ 10^{-3}$ (sub-critical, dashed line), $K = K_c = 4.2\ 10^{-3}$ (critical iso-K, dotted line) and $K = 5.9\ 10^{-3}$ (super-critical, continuous line). The circled numbers, arrows and horizontal lines indicate the yielding transition, see text for details. Color shades and color bar: probability distribution of the local relaxation rates Γ_i in simulations of the model with disorder and parameters chosen to reproduce the data for the microgels M2s shown in Fig. 2d: $K = 4\ 10^{-3}$, $1/\tau_0 = 2\ 10^{-5}$ s^{-1}, $\bar{\alpha} = 9\ 10^{-8}$, variance of $\alpha_{i,j} = 8.9\ 10^{-16}$, $n = 3$, $\omega = \pi$ rad s^{-1}. b): Probability distribution of the local relaxation rate for strain amplitudes corresponding to the fluid (blue), coexistence (gray) and solid-like (red) regimes, same colors as the corresponding horizontal lines in a). c): Snapshot of the simulated system corresponding to the bimodal distribution in b), showing the coexistence of regions with low (dark shades) and high (light shades) relaxation rates. In b) and c), the parameters are the same as for the model with disorder in a).

applied strain supports the model and highlights that disorder is indeed at the origin of the dynamic coexistence spanning a finite range of γ_0.

One of the most powerful consequences of VdW's theory is the law of corresponding states, predicting identical properties for distinct fluids, provided that they all have the same pressure, volume, and temperature relative to the corresponding values at the critical point.

Inspired by the law of corresponding states, we re-express Eq. 3 using reduced variables:

$$\left(\Gamma_r - \frac{1}{3}\right)\left({\gamma_r}^{-n} + \frac{3}{{\Gamma_r}^2}\right) = \frac{8}{3}K_r\,, \tag{4}$$

where $\Gamma_r = \Gamma/\Gamma_c$, $\gamma_r = \gamma_0/\gamma_{0,c}$, $K_r = K/K_c$, and where the values of the various parameters at the critical point, designated by the subscript c, are given in Table I. For the mean-field model, the coordinates of the critical point are derived by imposing that both the first and the second derivative of $\gamma_0(\Gamma)$ vanish, in analogy to VdW's equation of state. For the model with disorder, we use reduced variables obtained from Table I with the mean-field α replaced by the average value $\bar{\alpha}$ of the site-dependent $\alpha_{i,j}$.

$\gamma_{0,c}$	Γ_c	K_c
$\left(\frac{27}{\alpha\omega^2\tau_0^2}\right)^{1/n}$	$\frac{3}{\omega\tau_0}$	$\frac{8\alpha\omega\tau_0}{27}$

TABLE I. Values of the strain amplitude γ_0, relaxation rate Γ and K parameter at the critical point as predicted by the mean field model for the yielding transition.

Figure 4a shows the unified yielding state diagram for soft colloids obtained using reduced variables. For each sample, we tune $\bar{\alpha}$ and the variance σ_α^2 of the coupling constants distribution, the spontaneous relaxation rate $1/\tau_0$ and the exponent n in order to reproduce the strain dependence of $\Gamma_{s,f}$ and χ, as exemplified in Fig. 2d-f. Using these fitting parameters, we re-express the experimental variables in terms of the reduced variables of Fig. 4a. In this representation, all samples fall on nearly the same solid and fluid branches, characterized respectively by a single, compressed exponential slow mode (small Γ_r, blue solid symbols in Fig. 4a) and a single, fast stretched exponential mode (large Γ_r, red open symbols). This collapse is remarkable, given the diversity of the microscopic structure of the investigated samples, which in turn results in marked differences in the sensitivity to shear, compare e.g. the steep growth of Γ_s with applied strain for the emulsions to the gentler increase for microgels and nanoparticles (Figs. 2d-f). Furthermore, by analyzing data at various q vectors for E samples, we find that the collapse is robust with respect to the choice of the probed length scale, see Supplementary. At intermediate Γ_r, within the region inaccessible to the mean field model, a fast mode and a slow mode coexist (gray half-filled symbols in Fig. 4a), as predicted by the model with disorder; the abscissa used for these points is the weighted average of the fast and slow relaxation rates (see Methods).

In the coexisting region, samples' properties vary markedly and systematically with K_r, which suggests classifying all systems according to this parameter. Since $K_r < 1$ corresponds to glassy samples and $K_r > 1$ to equilibrated fluids, we quantify 'glassiness' of samples with $K_r < 1$ by $g = 1 - K_r$, which increases as the iso-K_r curves move downward (see arrow in Fig. 4a) away from the critical curve ($g = 0$, $K_r = 1$). For samples of the same kind, the trend in g (see Fig. 4b and Table SI2 in Supplementary) agrees with the behavior intuitively associated with a lesser or greater glassiness. For emulsions and microgels, we find that in general the higher φ the more glassy the sample. Consistent with the notion that with age systems evolve towards deeper states in the glassy phase, we find that g increases with age for sample N41%. Finally, one expects g to increase with ω, because glassy samples fall increasingly out of equilibrium as the time scale of the driving becomes shorter. This is indeed what is seen in our experiments, compare samples M40s and M2s. Beyond these comparisons, the notion of glassiness paves the way for a quantitative comparison between samples of different nature (e.g. emulsions *vs* microgels) or probed according to different protocols. Keeping in mind that each iso-K_r curve –and thus each g value– is characterized by a different disorder parameter of the coupling constants $d = \sigma_\alpha^2/\bar{\alpha}^2$, we find a remarkable negative correlation between the glassiness and d, which, as shown in Fig. 4b, is characterized by a simple master curve.

The correlation between glassiness and disorder has also deep implications on the nature of the yielding transition. We find that the most glassy samples, for which d approaches the $d = 0$ mean field limit, exhibit features typical of a first-order transition, as predicted by the mean field model (Fig. 5a-c). Figure 5a shows w, the relative width of the γ_0 range where fast and slow modes coexists in experiments, demonstrating a dramatic increase of the transition sharpness as d decreases. Figures 5b-c demonstrate hysteresis, another distinctive feature of first-order transitions (data from simulations). As seen in Fig. 5c, hysteresis is largest for the smallest disorder and vanishes when departing from the mean field limit.

Conversely, systems close to the critical K and hence with large d (small g) exhibit features usually associated with second order transitions, illustrated in Fig. 5d-f. Figure 5d shows for sample M2s that temporal fluctuations of the relaxation rate are strongly enhanced at the transition. Figures 5e-f demonstrate sluggishness, another feature of second-order transitions: in both experiments (Fig. 5e) and simulations (Fig. 5f) on systems with large d (small g), the time to attain a stationary state dramatically increases around the transition.

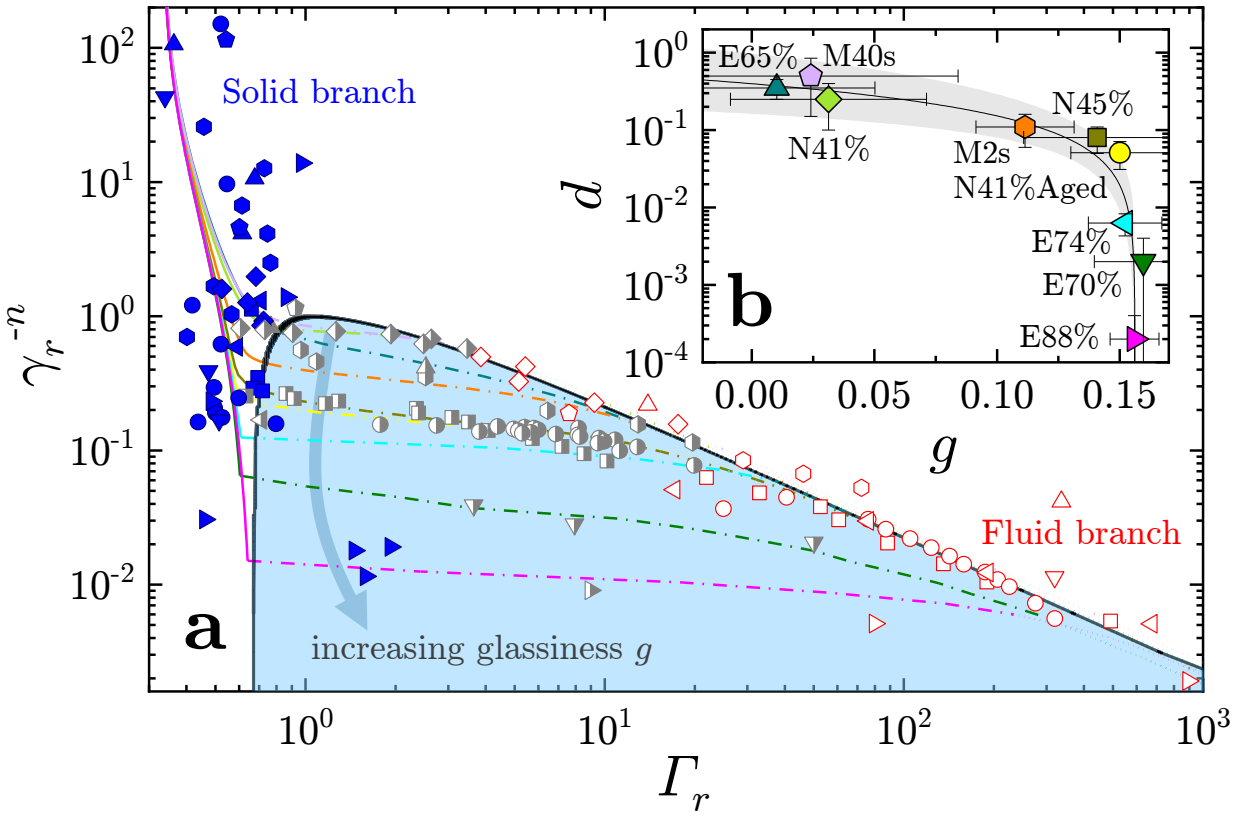

FIG. 4. **Unified state diagram for the yielding transition.** a): Yielding state diagram for all samples, using reduced variables (see text). Blue, solid (resp., red, open) symbols: samples with a single slow (resp., fast) relaxation mode. Gray half-filled symbols: coexistence of the slow and fast modes. The symbol shape is the same as in b), where the samples are identified by labels, see Methods. The continuous, dotted and dash-dotted lines indicate the solid, fluid and coexistence branches of the iso-K lines obtained from simulations of the model with disorder (same color codes as in b)). Area shaded in light blue below the black line: region inaccessible to the mean field model, corresponding to the coexistence of fast and slow relaxation modes in experiments and simulations of the model with disorder. b): Disorder $d = \sigma_\alpha^2/\bar{\alpha}^2$ of the coupling constants $\alpha_{i,j}$ (see Eq. 2) as a function of 'glassiness', defined as the reduced distance form the critical point, $g = 1 - K_r$ (see also the arrow in a)).

The unified yielding state diagram established here demonstrates the universal nature of the solid-fluid transition in soft glassy systems under oscillatory shear. Our model differs from previous approaches by introducing a direct link between the macroscopic drive and the microscopic dynamics, and by including in the latter the contribution of ultra-slow,

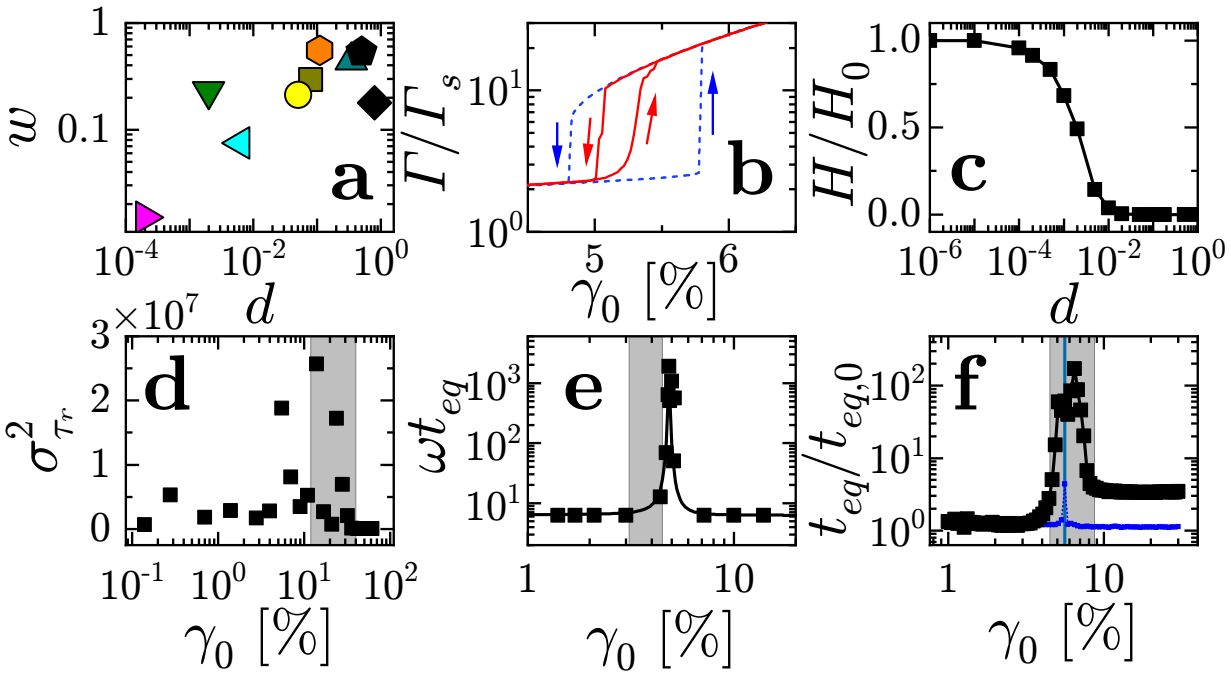

FIG. 5. **Distance from a critical point governs the nature of the yielding transition.** Top row: features typical of a first order transition are enhanced as glassiness increases (d decreases). a): Relative width w of the transition in experiments probing the microscopic dynamics across yielding (see Methods for details). b): Hysteresis at yielding, data from simulations with $d = 0$ (dashed lines, blue shades) and $d = 0.02$ (solid lines, red shades). c): Area H of the hysteresis loop in simulations with disorder, normalized by that in the $d = 0$ limit. Bottom row: features typical of a second order transition emerge close to the critical point (small g, large d). d): Fluctuations of the dynamics, quantified by the temporal variance $\sigma^2_{\tau_r}$ of the relaxation time of the intensity correlation functions, are strongly enhanced at the transition. Data for sample M2s. e): Normalized time $t_{eq}\omega$ to attain stationary dynamics for sample N41%. The lines are a guide to the eye. f): Number of iterations required for numerical solutions of the model with disorder to converge. Data are normalized by their corresponding value at $d = 0$. Black symbols and line: $d = 0.1$; blue line: $d = 10^{-4}$. In d)-f), the gray shaded area indicates the range of the dynamical transition (see Methods for details). Panels b, c, f: same mean field parameters as in Figs. 2b,e.

spontaneous relaxations; as a result, slow and fast relaxation modes may coexist. These two modes might be associated with the formation of shear bands organized in the shear gradient direction [42, 43]. Our light scattering experiments cannot test directly this hypothesis;

however, our numerical data, microscopy experiments on emulsions, and photon correlation imaging measurements on sample N45% are inconsistent with shear banding (Supplementary Sec. IV), rather pointing to the formation of fast-relaxing domains similar to those of Fig. 3c. This suggests that the coexistence of slow- and fast-relaxing regions is a generic feature, not necessarily implying the structuration in shear bands. A key result of our work is the emergence of different features in the transition depending on the distance from the critical point. This indicates a promising way to reconcile apparently conflicting reports in previous studies of yielding.

Finally, the model proposed here does not depend on the details of the interaction between the microscopic constituents of the system: we thus expect it to provide a general framework for the yielding transition, possibly including in systems with attractive interactions [44, 45].

METHODS

Samples

Table II summarizes the main sample and experimental parameters. PNIPAM microgels (M) were synthesized by emulsion polymerization as described in [46], and were suspended in a 2 mM NaN_3 aqueous solution to prevent bacterial growth. The microgel radius at $T = 23$ °C is 294 nm, as measured by dynamic light scattering (DLS) in a diluted suspension. Sample preparation and characterization, including the determination of the effective volume fraction φ, are described in [47]. Note that the effective volume fraction is larger than one, due to the particle softness. Charged nanoparticle systems (N) were prepared by concentrating an acqueous suspension of silica particles (Ludox TM50, from Sigma Aldrich), as described in [47]. The particles have a hydrodynamic radius of 23 nm, as measured by DLS in the dilute limit. To improve the scattering signal, the samples were seeded with 200 nm-diameter polystyrene particles at extremely low volume fraction, $\phi_{PS} < 10^{-6}$. We check that this seeding has no measurable impact on the rheological properties microscopic dynamics of the samples. Concentrated emulsions (E) were prepared by dispersing polydimethylsiloxane droplets into a water/glycerol matrix, as described in [4]. The resulting droplets have an average size of 2.4 μm and 20% polydispersity. All samples were initialized

by applying a preshear, see Sec. IIa of the Supplementary for details. Rheology and microscopic dynamics started immediately after applying the preshear for all samples, except for sample N41%Aged, which was left at rest for 12h prior to measurements.

Sample ID	φ	T (s)	ω [rad/s]	q [μm^{-1}]	setup	**q** orientation
M2s	1.5	2	3.14	5	PCI	vorticity
M40s	1.5	40	0.157	0.1-5	SALS	vorticity
N41%	0.41	2	3.14	30	PCI	shear gradient
N41%Aged	0.41	2	3.14	30	PCI	shear gradient
N45%	0.45	2	3.14	30	PCI	shear gradient
E65%	0.65	1	6.28	1-20	ff-DDM	vorticity
E70%	0.70	1	6.28	1-20	ff-DDM	vorticity
E74%	0.74	1	6.28	1-20	ff-DDM	vorticity
E88%	0.88	1	6.28	1-20	ff-DDM	vorticity

TABLE II. Main features of the samples used in this study. M, N, and E refer to microgels, nanoparticles and emulsions, respectively. φ designates the volume fraction for N and E, and the effective volume fraction for M, as defined in [47]. T is the period of the oscillatory strain. PCI, SALS, and ff-DDM are photon correlation imaging, small angle light scattering and far field differential dynamic microscopy, respectively. The last column shows the orientation of the largest component of **q** with respect to the shear field, see *Experimental setups* for details.

Experimental setups

With the only exception of E samples, all experiments are performed with a home-made shear cell equipped with sliding parallel plates [48], sketched in Supplementary Fig. SI2. One plate is driven by a piezoelectric strain actuator (P602, from Physik Instrumente) and a force sensor (LC601, from Omega Engineering) measures the force applied by the actuator, enabling strain-controlled rheology experiments. The sample has a cross-sectional area of about 4 cm^2 and a thickness between 300 and 700 μm. For most experiments, shear rheology was coupled to a spatially-resolved Photon Correlation Imaging (PCI) apparatus [49], collecting light scattered in a direction orthogonal to the shear and forming a scattering

angle θ with the incoming beam. For samples N, we choose $\theta = 141°$, yielding a scattering vector $q = 4\pi n_r \lambda^{-1} \sin(\theta/2) = 30\ \mu\text{m}^{-1}$, where $n_r = 1.33$ is the solvent refractive index and $\lambda = 532.5$ nm the wavelength of laser light. In this case, q is predominantly oriented along the shear gradient direction, with a minor component $q_x = 3\ \mu\text{m}^{-1}$ along the vorticity direction. For M2s, we choose $\theta = 20°$ such that $q = 5\ \mu\text{m}^{-1}$ is predominantly oriented along the vorticity direction, with a minor component $q_z = 0.9\ \mu\text{m}^{-1}$ along the shear gradient. For M40s, experiments are performed using a different scattering geometry: a far-field small angle light scattering apparatus (SALS) enabling multiple scattering vectors to be probed simultaneously, oriented along both the velocity and the vorticity direction, with $0.1\ \ \mu\text{m}^{-1} \leq q \leq 5\ \ \mu\text{m}^{-1}$. Data shown in the main text correspond to $q = 4.8\ \ \mu\text{m}^{-1}$, oriented along the vorticity direction. See Supplementary Figs SI1-SI3 for the schemes of the setups.

For samples E, a different home-made shear cell with parallel, counter-translating plates displaced by a piezoelectric actuator is coupled to an inverted microscope with differential interference contrast (DIC) optics [4] , see Supplementary Fig. SI3. The acquired imaged region has a depth of field of $0.5\ \ \mu$m, much smaller than the droplet size, and the imaged plane corresponds to the stagnation plane of the shear deformation. We analyze microscopy videos using far-field Differential Dynamic Microscopy (ff-DDM) [50], which yields an intensity correlation function equivalent to DLS, with scattering vectors $1\ \ \mu\text{m}^{-1} \leq q \leq 20\ \ \mu\text{m}^{-1}$ in the velocity-vorticity plane. Data presented in the main text correspond to $q = 9\ \ \mu\text{m}^{-1}$ along the vorticity direction. Data for more scattering vectors are included in Supplementary Fig. SI6-SI9.

Characterization of the microscopic dynamics

We quantify the microscopic dynamics via the two-time intensity correlation $g_2(t,\tau)-1 = \beta\langle I_p(t)I_p(t+\tau)\rangle/[\langle I_p(t)\rangle\langle I_p(t+\tau)\rangle]$, with β a constant such that $g_2(t,\tau)-1 \to 1$ for $\tau \to 0$. I_p is the scattered intensity collected by the $p-th$ pixel of the detector (for the PCI and SALS setups), or a component of the Fourier transform of the microscope images for sample E. $\langle \dots \rangle$ indicates the average over a set of pixels corresponding nearly to the same scattering vector or Fourier component.

In the stationary regime, we average $g_2 - 1$ over time t to reduce noise before fitting

Eq. 1 to the data. In Fig. 4a, the abscissa of the state points belonging to the coexistence region is calculated as the weighted average of the slow and fast relaxation rates, normalized by the relaxation rate at the critical point: $\Gamma_r = [\chi\Gamma_s + (\chi - 1)\Gamma_f]/\Gamma_c$. The slow and fast relaxation rates are obtained by fitting Eq. 1 to the experimental $g_2 - 1$.

To quantify the temporal fluctuations of the dynamics, we inspect the t-dependence of the two-time correlation functions, with no t averaging performed on $g_2(t, \tau) - 1$. For each t, a relaxation time $\tau_r(t)$ is obtained from $\tau_r = \int_0^\infty [g_2(t, \tau) - 1]\mathrm{d}\tau$, a procedure more robust than fitting to Eq. 1 when dealing with correlation functions that are not averaged over t and are thus more noisy. In Fig. 5d we show $\sigma^2_{\tau_r}$, the temporal variance of $\tau_r(t)$.

We locate the range of the dynamic transition by determining the two strain amplitudes $\gamma_{0,s}$ and $\gamma_{0,e}$ such that $0.05 \leq \chi \leq 0.95$ for $\gamma_{0,s} \leq \gamma_0 \leq \gamma_{0,e}$. The gray shaded regions in Figs. 5d-f highlight the strain range $\gamma_{0,s} \leq \gamma_0 \leq \gamma_{0,e}$. The normalized width of the transition shown in Fig. 5a is defined as $w = (\gamma_{0,e} - \gamma_{0,s})/(\gamma_{0,e} + \gamma_{0,s})$.

Numerical solution of the model with disorder

To study the effect of disorder on yielding, we implement our model (Eq. 2) on a D-dimensional cubic lattice with periodic boundary conditions. Each site, i, is assigned a local relaxation rate, Γ_i, and each pair of neighbor sites is attributed a coupling constant, α_{ij}, randomly drawn from a probability distribution, $P(\alpha)$. For a given strain amplitude γ_0 and starting from an initial configuration of local rates $\Gamma_i^{(init)}$, we seek a configuration of local rates $\Gamma_i^{(sol)}$ that satisfies Eq. 2 for all sites. In our implementation, $\Gamma_i^{(sol)}$ is approached iteratively: at each step, a set of target site rates $\Gamma_i^{(t)}$ is computed through Eq. 2 using the current site rates $\Gamma_i^{(c)}$. $\Gamma_i^{(t)}$ then replaces $\Gamma_i^{(c)}$ for the following iteration, yielding a new set of target site rates. The convergence criterion is expressed in terms of a loss function $\mathcal{L} = \sum_i \left[\left(\log \Gamma_i^{(c)} - \log \Gamma_i^{(t)} \right) / \log \Gamma_i^{(t)} \right]^2$, which tends to 0 as $\Gamma_i^{(c)}$ approaches $\Gamma_i^{(sol)}$.

Results shown in this paper are obtained for $D = 2$ and a Log-Normal distribution of the coupling constants: $P(\alpha; \mu, \sigma) = (\alpha\sigma\sqrt{2\pi})^{-1} \exp[-(\ln \alpha - \mu)^2/(2\sigma^2)]$, where the average $\bar{\alpha}$ and variance σ^2_α of the coupling constants are related to the parameters μ, σ of the Log-Normal distribution by $\bar{\alpha} = \exp(\mu + \sigma^2/2)$ and $\sigma^2_\alpha = \bar{\alpha}^2(\exp \sigma^2 - 1)$. We quantify disorder by the dimensionless parameter $d = \sigma^2_\alpha/\bar{\alpha}^2$. Representative results for different choices of $P(\alpha)$ are shown in Supplementary Fig. SI13, and exhibit no qualitative differences.

To mimic the effect of preshear in experiments, the iterative solution of the numerical model is typically initiated with a uniform distribution of local rates $\Gamma_i^{(init)} = \Gamma^{(0)}$. The effect of hysteresis shown in Figs. 5b,c is studied by simulating an amplitude sweep experiment: γ_0 is first increased from low to high amplitudes and then decreased from high to low amplitudes, every time initiating the iterative calculation from the model solution for the previous amplitude.

DATA AVAILABILITY

The data that support the plots within this paper and other findings of this study are available from the corresponding authors upon request.

CODE AVAILABILITY

The code that support the plots within this paper and other findings of this study are available from the corresponding authors upon request.

---

[1] D. Bonn, M. M. Denn, L. Berthier, T. Divoux, and S. Manneville, Yield Stress Materials in Soft Condensed Matter, Rev. Mod. Phys. **89**, 035005 (2017).

[2] N. Koumakis, J. F. Brady, and G. Petekidis, Complex Oscillatory Yielding of Model Hard-Sphere Glasses, Physical Review Letters **110**, 178301 (2013).

[3] T. G. Mason, J. Bibette, and D. A. Weitz, Yielding and flow of monodisperse emulsions, Journal of Colloid and Interface Science **179**, 439 (1996).

[4] E. D. Knowlton, D. J. Pine, and L. Cipelletti, A microscopic view of the yielding transition in concentrated emulsions, Soft Matter **10**, 6931 (2014).

[5] M. C. Rogers, K. Chen, M. J. Pagenkopp, T. G. Mason, S. Narayanan, J. L. Harden, and R. L. Leheny, Microscopic signatures of yielding in concentrated nanoemulsions under large-amplitude oscillatory shear, Physical Review Materials **2**, 095601 (2018).

[6] S. A. Rogers, B. M. Erwin, D. Vlassopoulos, and M. Cloitre, Oscillatory yielding of a colloidal star glass, Journal of Rheology **55**, 733 (2011).

[7] R. J. Ketz, R. K. Prud'homme, and W. W. Graessley, Rheology of concentrated microgel solutions, Rheol Acta **27**, 531 (1988).

[8] P. Sollich, F. Lequeux, P. Hébraud, and M. E. Cates, Rheology of soft glassy materials, Physical Review Letters **78**, 2020 (1997).

[9] J. R. Seth, L. Mohan, C. Locatelli-Champagne, M. Cloitre, and R. T. Bonnecaze, A micromechanical model to predict the flow of soft particle glasses, Nature Materials **10**, 838 (2011).

[10] G. J. Donley, P. K. Singh, A. Shetty, and S. A. Rogers, Elucidating the G″ overshoot in soft materials with a yield transition via a time-resolved experimental strain decomposition, Proc Natl Acad Sci USA **117**, 21945 (2020).

[11] J. M. Brader, M. Siebenbürger, M. Ballauff, K. Reinheimer, M. Wilhelm, S. J. Frey, F. Weysser, and M. Fuchs, Nonlinear response of dense colloidal suspensions under oscillatory shear: Mode-coupling theory and fourier transform rheology experiments, Physical Review E **82**, 061401 (2010).

[12] T. Voigtmann, Nonlinear glassy rheology, Current Opinion in Colloid & Interface Science **19**, 549–560 (2014).

[13] G. Picard, A. Ajdari, L. Bocquet, and F. Lequeux, Simple model for heterogeneous flows of yield stress fluids, Physical Review E **66**, 051501 (2002).

[14] R. Benzi, T. Divoux, C. Barentin, S. Manneville, M. Sbragaglia, and F. Toschi, Unified Theoretical and Experimental View on Transient Shear Banding, Phys. Rev. Lett. **123**, 248001 (2019).

[15] C. Liu, K. Martens, and J.-L. Barrat, Mean-Field Scenario for the Athermal Creep Dynamics of Yield-Stress Fluids, Phys. Rev. Lett. **120**, 028004 (2018).

[16] R. Sainudiin, M. Moyers-Gonzalez, and T. Burghelea, A microscopic Gibbs field model for the macroscopic yielding behaviour of a viscoplastic fluid, Soft Matter **11**, 5531 (2015).

[17] N. C. Keim and P. E. Arratia, Yielding and microstructure in a 2D jammed material under shear deformation, Soft Matter **9**, 6222 (2013).

[18] D. Fiocco, G. Foffi, and S. Sastry, Oscillatory athermal quasistatic deformation of a model glass, Physical Review E **88**, 020301 (2013).

[19] K. Hima Nagamanasa, S. Gokhale, A. K. Sood, and R. Ganapathy, Experimental signatures of a nonequilibrium phase transition governing the yielding of a soft glass, Physical Review E **89**, 10.1103/PhysRevE.89.062308 (2014).

[20] R. Jeanneret and D. Bartolo, Geometrically protected reversibility in hydrodynamic Loschmidt-echo experiments, Nat Commun **5**, 3474 (2014).

[21] T. Kawasaki and L. Berthier, Macroscopic yielding in jammed solids is accompanied by a nonequilibrium first-order transition in particle trajectories, Physical Review E **94**, 022615 (2016).

[22] P. Leishangthem, A. D. S. Parmar, and S. Sastry, The yielding transition in amorphous solids under oscillatory shear deformation, Nat Commun **8**, 14653 (2017).

[23] P. Edera, M. Brizioli, G. Zanchetta, G. Petekidis, F. Giavazzi, and R. Cerbino, Deformation profiles and microscopic dynamics of complex fluids during oscillatory shear experiments, Soft Matter **17**, 8553–8566 (2021).

[24] S. Lerouge and J.-F. Berret, Shear-Induced Transitions and Instabilities in Surfactant Wormlike Micelles, in *Polymer Characterization*, Vol. 230, edited by K. Dusek and J.-F. Joanny (Springer Berlin Heidelberg, Berlin, Heidelberg, 2009) pp. 1–71.

[25] L. Cipelletti, L. Ramos, S. Manley, E. Pitard, D. A. Weitz, E. E. Pashkovski, and M. Johansson, Universal non-diffusive slow dynamics in aging soft matter, Faraday Discuss. **123**, 237 (2003).

[26] A. Madsen, R. L. Leheny, H. Guo, M. Sprung, and O. Czakkel, Beyond simple exponential correlation functions and equilibrium dynamics in x-ray photon correlation spectroscopy, New Journal of Physics **12**, 055001 (2010).

[27] D. V. Denisov, M. T. Dang, B. Struth, A. Zaccone, G. H. Wegdam, and P. Schall, Sharp symmetry-change marks the mechanical failure transition of glasses, Scientific Reports **5**, 14359 (2015).

[28] T. Divoux, V. Grenard, and S. Manneville, Rheological Hysteresis in Soft Glassy Materials, Physical Review Letters **110**, 018304 (2013).

[29] L. Bocquet, A. Colin, and A. Ajdari, Kinetic Theory of Plastic Flow in Soft Glassy Materials, Physical Review Letters **103**, 036001 (2009).

[30] K. N. Nordstrom, J. P. Gollub, and D. J. Durian, Dynamical heterogeneity in soft-particle suspensions under shear, Physical Review E **84**, 021403 (2011).

[31] P. Hebraud, F. Lequeux, J. P. Munch, and D. J. Pine, Yielding and Rearrangements in Disordered Emulsions, Phys. Rev. Lett. **78**, 4657 (1997).

[32] W. van Megen, T. C. Mortensen, S. R. Williams, and J. Muller, Measurement of the self-intermediate scattering function of suspensions of hard spherical particles near the glass transition, Phys. Rev. E **58**, 6073 (1998).

[33] E. R. Weeks, J. C. Crocker, A. C. Levitt, A. Schofield, and D. A. Weitz, Three-dimensional direct imaging of structural relaxation near the colloidal glass transition, Science **287**, 627 (2000).

[34] C. Derec, A. Ajdari, and F. Lequeux, Rheology and aging: A simple approach, The European Physical Journal E: Soft Matter and Biological Physics **4**, 355 (2001).

[35] K. Miyazaki, H. M. Wyss, D. A. Weitz, and D. R. Reichman, Nonlinear viscoelasticity of metastable complex fluids, Europhysics Letters (EPL) **75**, 915 (2006).

[36] A. Hess and N. Aksel, Yielding and structural relaxation in soft materials: Evaluation of strain-rate frequency superposition data by the stress decomposition method, Physical Review E **84**, 051502 (2011).

[37] G. Biroli and J. P. Garrahan, Perspective: The glass transition, The Journal of Chemical Physics **138**, 12A301 (2013).

[38] J. Zausch, J. Horbach, M. Laurati, S. U. Egelhaaf, J. M. Brader, T. Voigtmann, and M. Fuchs, From equilibrium to steady state: the transient dynamics of colloidal liquids under shear, Journal of Physics: Condensed Matter **20**, 404210 (2008).

[39] S. Aime *et al.*, Microscopic yielding of glassy materials under oscillatory shear.

[40] A. N. Berker, Critical behavior induced by quenched disorder, Physica A: Statistical Mechanics and its Applications **194**, 72–76 (1993).

[41] A. Bellafard, S. Chakravarty, M. Troyer, and H. G. Katzgraber, The effect of quenched bond disorder on first-order phase transitions, Annals of Physics **357**, 66–78 (2015).

[42] T. Divoux, M. A. Fardin, S. Manneville, and S. Lerouge, Shear banding of complex fluids, Annual Review of Fluid Mechanics **48**, 81–103 (2016).

[43] R. Radhakrishnan and S. M. Fielding, Shear Banding of Soft Glassy Materials in Large Amplitude Oscillatory Shear, Physical Review Letters **117**, 188001 (2016).

[44] K. N. Pham, A. M. Puertas, J. Bergenholtz, S. U. Egelhaaf, A. Moussaid, P. N. Pusey, A. B. Schofield, M. E. Cates, M. Fuchs, and W. C. K. Poon, Multiple glassy states in a simple model system, Science **296**, 104 (2002).

[45] T. Gibaud, D. Frelat, and S. Manneville, Heterogeneous yielding dynamics in a colloidal gel, Soft Matter **6**, 3482 (2010).

[46] D. Truzzolillo, S. Sennato, S. Sarti, S. Casciardi, C. Bazzoni, and F. Bordi, Overcharging and reentrant condensation of thermoresponsive ionic microgels, Soft Matter **14**, 4110 (2018).

[47] A.-M. Philippe, D. Truzzolillo, J. Galvan-Myoshi, P. Dieudonné-George, V. Trappe, L. Berthier, and L. Cipelletti, Glass transition of soft colloids, Physical Review E **97**, 040601(R) (2018).

[48] S. Aime, L. Ramos, J. M. Fromental, G. Prévot, R. Jelinek, and L. Cipelletti, A stress-controlled shear cell for small-angle light scattering and microscopy, Review of Scientific Instruments **87**, 123907 (2016).

[49] L. Cipelletti, V. Trappe, and D. J. Pine, Scattering Techniques, in *Fluids, Colloids and Soft Materials*, edited by A. Fernandez-Nieves and A. Puertas (John Wiley & Sons, Inc., 2016) pp. 131–148.

[50] S. Aime and L. Cipelletti, Probing shear-induced rearrangements in Fourier space. II. Differential dynamic microscopy, Soft Matter **15**, 213 (2019).

ACKNOWLEDGMENTS

We thank E. D. Knowlton for help with the experiments on emulsions and L. Berthier for illuminating discussions. This work was funded by the French CNES, ANR (grants No. ANR-14-CE32-0005, FAPRES, and ANR-20-CE06-0028, MultiNet), and by the EU (Marie Sklodowska-Curie ITN Supolen Grant 607937). LC acknowledges support from the Institut Universitaire de France.

AUTHOR CONTRIBUTIONS

SA, LR, DJP, and LC designed experiments. SA performed experiments and numerical simulations. SA and DT conceived the model. All authors analyzed the results, discussed and improved the model, and contributed to writing the paper.

COMPETING INTERESTS

The authors declare no competing interests.

ADDITIONAL INFORMATION

Supplementary information The online version contains supplementary material available at [url to be inserted].

Correspondence and requests for materials should be addressed to SA or LC.

SUPPLEMENTARY INFORMATION TO "A UNIFIED STATE DIAGRAM FOR THE YIELDING TRANSITION OF SOFT COLLOIDS"

Stefano Aime*,[1,2] Domenico Truzzolillo,[1] David J. Pine,[3] Laurence Ramos,[1] and Luca Cipelletti*[1,4]

[1] *Laboratoire Charles Coulomb (L2C), Université Montpellier, CNRS, Montpellier, France*

[2] *Present address: ESPCI, Paris, France**

[3] *New York University*

[4] *Institut Universitaire de France*†

TABLE OF CONTENTS

Supplementary information to "A unified state diagram for the yielding transition of soft colloids" 1
Table of contents 1
I. Experimental setups 2
II. Additional experimental data and fit parameters 5
II.a Experimental and fit parameters 5
II.b Strain amplitude dependence of the viscoelastic moduli 6
II.c Dynamics at rest or in the $\gamma_0 \to 0$ limit 7
II.d Scattering vector dependence of the dynamics and of the model parameters 8
II.e Impact of the oscillatory frequency (samples M2s and M40s) 13
III. Numerical model 14
IV. Spatial heterogeneity of the dynamics and shear bands 17
References 20

I. EXPERIMENTAL SETUPS

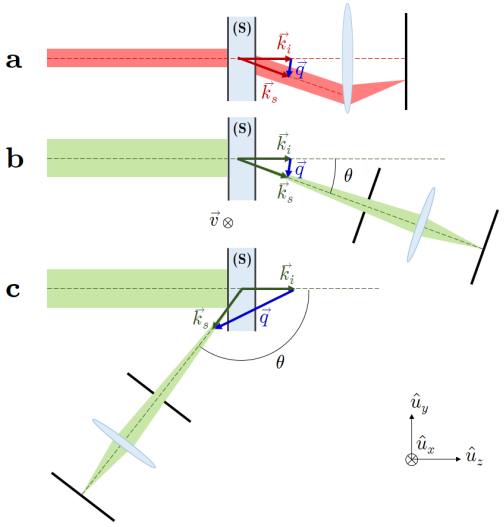

Figure SI1: Sketch of dynamic light scattering (DLS [1]) setups.

a) Far-field light scattering setup used for sample M40s: the detector is in the focal plane of the lens. b) Small-angle Photon Correlation Imaging (PCI) setup used for sample M2s: the lens images the sample S onto the detector; only light scattered at angles near to the scattering angle θ contributes to the image formation. c) Wide-angle PCI setup used for N samples: same imaging geometry as in b), but for a larger scattering angle. In all sketches, $\overrightarrow{\boldsymbol{u_x}}, \overrightarrow{\boldsymbol{u_y}}, \overrightarrow{\boldsymbol{u_z}}$ denote velocity, vorticity and gradient directions, respectively. $\overrightarrow{\boldsymbol{k_i}}, \overrightarrow{\boldsymbol{k_s}}$ and $\vec{\boldsymbol{q}}$ denote the incoming and scattered wave vectors and the scattering vector, respectively. The shear cell is not shown for clarity.

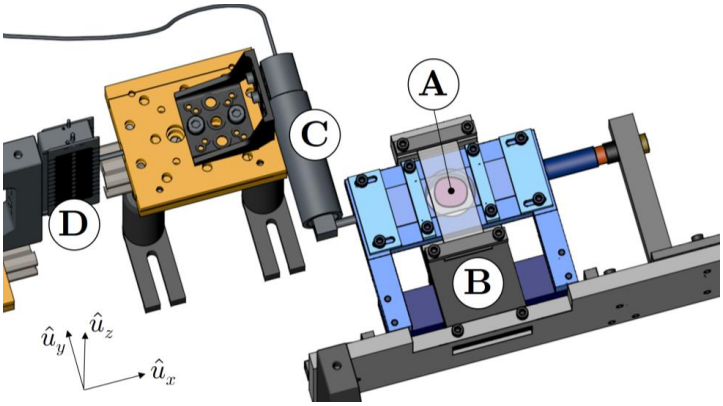

Figure SI2: Sketch of the custom shear cell for the DLS setups.

A) Sample, confined between two transparent parallel plates; B) shear cell, mounted on an air bearing stage [2] C) stress sensor (Model LC601, from Omega Engineering) D) strain piezoelectric actuator (P602, from Physik Instrumente). $\overrightarrow{\boldsymbol{u_x}}, \overrightarrow{\boldsymbol{u_y}}, \overrightarrow{\boldsymbol{u_z}}$ denote velocity, vorticity and gradient directions, respectively.

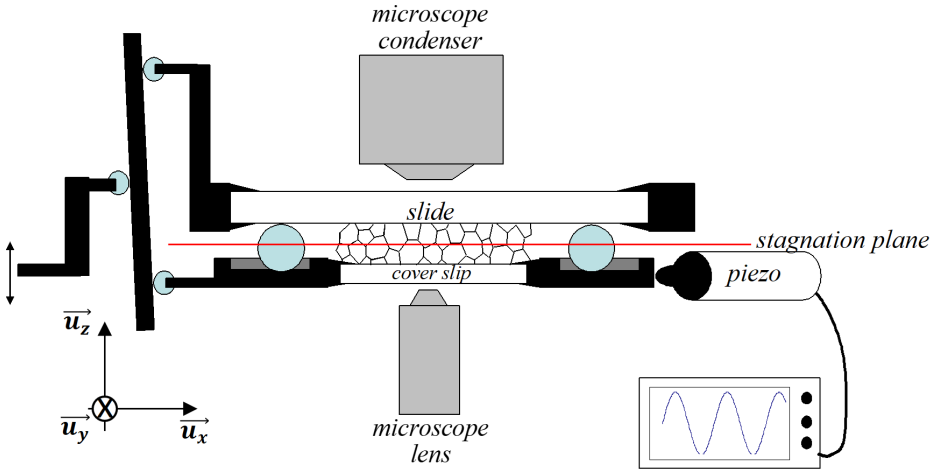

Figure SI3: Sketch of the custom shear cell for the emulsion samples.

The sample is imaged in the stagnation plane (indicated by the red line), which is at rest in the laboratory frame. $\overrightarrow{u_x}, \overrightarrow{u_y}, \overrightarrow{u_z}$ denote velocity, vorticity and gradient directions, respectively. Adapted from [3]. Data collected with this setup are analyzed using Digital Fourier Microscopy [4].

II. ADDITIONAL EXPERIMENTAL DATA AND FIT PARAMETERS

II.a Experimental and fit parameters

Sample	γ_{min}	γ_{max}	ν	β_0	$(1/\tau_0)/\ s^{-1}$	β_s	β_f	$\omega\Gamma_s/s^{-1}$
M2s	0.1%	62%	0.6	1.5	2.5×10^{-5}	1.3	0.33	2×10^{-5}
M40s	2.8%	69%	0.6	1.5	2.5×10^{-5}	1.6	0.44	2×10^{-5}
N41%	0.01%	72%	0.75	1.2	1.4×10^{-4}	1.4	0.36	1×10^{-4}
N41%Aged	0.01%	8.6%	0.75	1.2	1.4×10^{-4}	1.2	0.90	1×10^{-4}
N45%	1%	25%	0.7	1.9	1.2×10^{-4}	1.9	0.88	1.1×10^{-4}
E65%	0.4%	6.4%	0.6			1.5	0.34	1.6×10^{-3}
E70%	1.2%	6.4%	0.65			1.0	0.40	1.3×10^{-4}
E74%	4.8%	12%	0.65			1.4	0.32	6.1×10^{-4}
E88%	5.4%	20%	0.7			1.7	0.29	6.6×10^{-4}

Table SI1: Experimental and fit parameters for the probed samples.

Minimum (γ_{min}) and maximum (γ_{max}) applied strain deformations, terminal slopes ν of $G''(\gamma_0)$ defined in Fig. 1a of the main text, spontaneous relaxation rate $1/\tau_0$ and stretching exponents β_0, β_s, β_f of the fits to correlation functions (see main text for the definitions). The relaxation rates shown here are measured at representative scattering vectors q=5 μm^{-1}, 30 μm^{-1} and 9 μm^{-1} for M, N and E samples, respectively. For the M and N samples, β_0 and τ_0 are measured at rest. For the E samples, no correlation functions at rest are available, but β_s and $\omega\Gamma_s$ are obtained, as for the other samples shown in the table, in the low strain regime, where these parameters are essentially strain-independent and representative of the behavior at rest. For sample E70%, the decay of the correlation functions in the $\gamma_0 \rightarrow 0$ limit is modest, making it difficult to determine unambiguously β_s, whose value was thus set to unity.

Shear protocol: All samples were presheared before each measurement at a given γ_0, using oscillatory shear at the same ω as for the subsequent measurement. Samples E were presheared for several minutes at a high strain, typically 250–300%. The strain amplitude was then reduced to the target value and at least 300 cycles were imposed at the target γ_0 before starting the image acquisition, which lasted 1000 cycles or more. Samples M and N were presheared at the largest γ_0 to be tested. The preshear lasted 500 oscillations for sample M40s, 5000 for all other M and N samples. After presehar, shear at each amplitude had 2500 oscillations (sample M40s) or 50000 oscillations (all other M and N samples). We changed the order at which the various γ_0 values were tested (including by varying γ_0 non-monotonically), finding that our results did not depend on the specific sequence of tested strain amplitudes.

II.b Strain amplitude dependence of the viscoelastic moduli

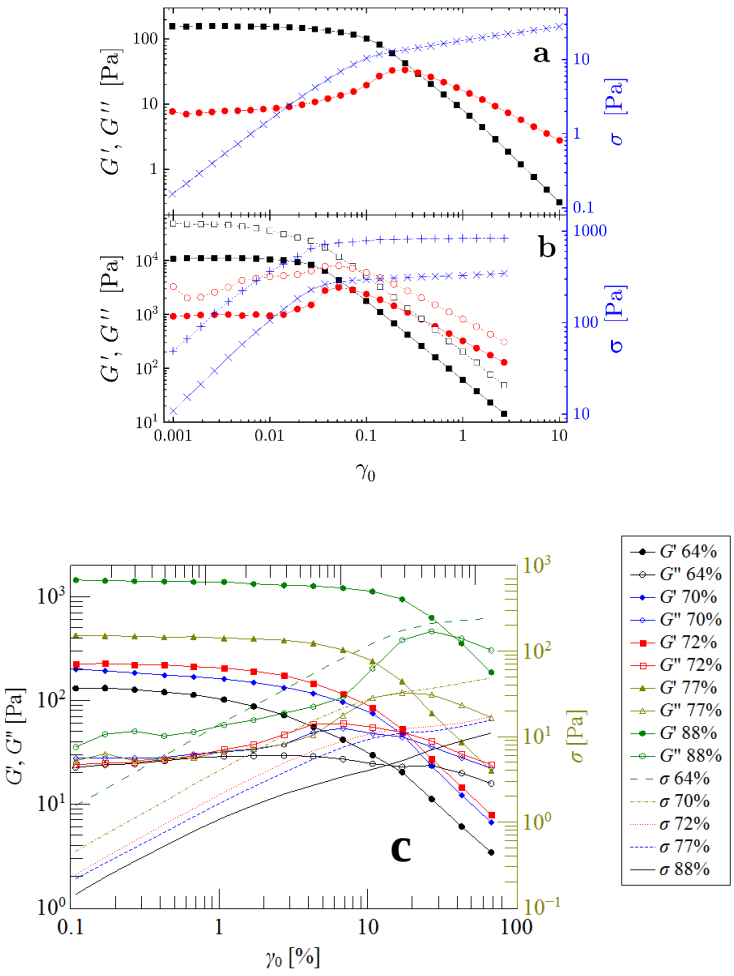

Figure SI4: Rheology data for all samples.

Dependence of the viscoelastic moduli G' and G" and of the shear stress σ on shear strain. a: microgels (same data as in Fig. 1 of the main text); b: nanoparticle samples, $\varphi = 43.5\%$ (solid symbols and crosses) and 46% (open symbols and pluses); c: emulsions [3]. In panels a and b, squares, circles and crosses or pluses correspond to G', G", and σ, respectively. Data in a were collected in the custom shear cell of Fig. SI2. All other data were obtained using a commercial rheometer. For the N and E samples, the volume fraction is slightly different from that of the corresponding samples used for light scattering and microscopy, which entails no significant difference in the rheological properties with respect to those shown here.

II.c Dynamics at rest or in the $\gamma_0 \rightarrow 0$ limit

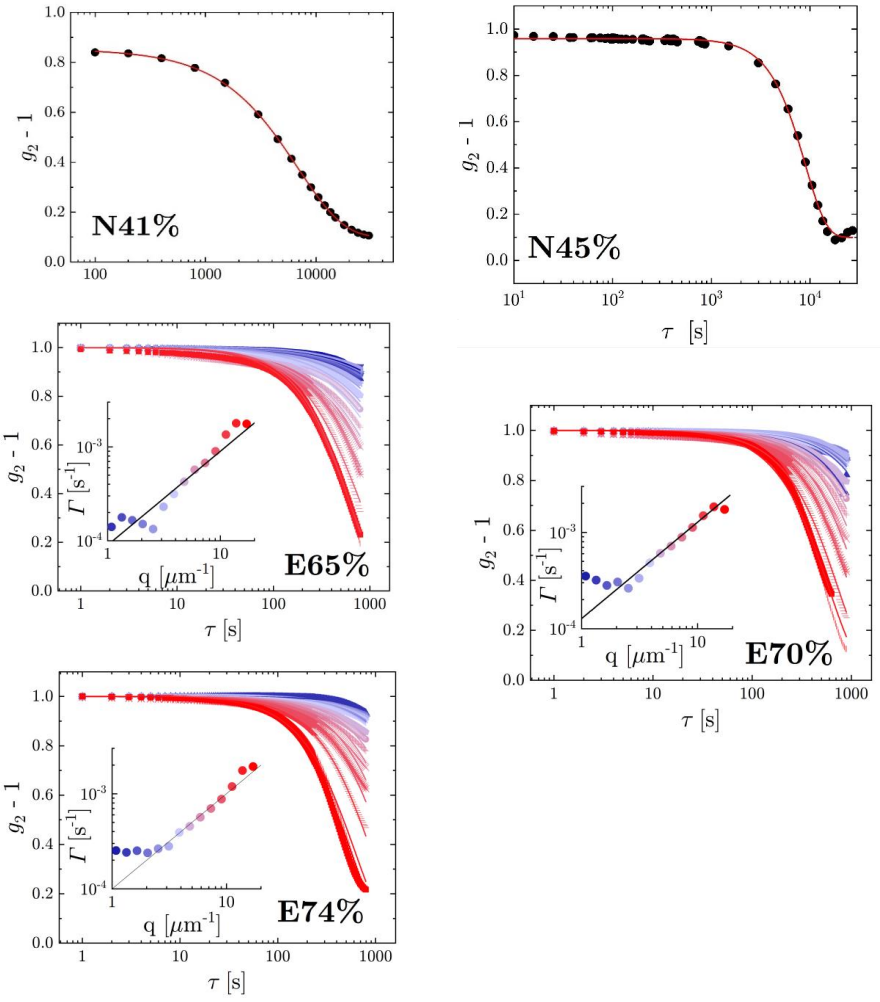

Figure SI5: Dynamics at rest or in the $\gamma_0 \rightarrow 0$ limit for N and E samples.

Intensity correlation functions for various N and E samples. For N samples, data are taken at rest. For E samples, data are taken in the low-strain regime where the dynamics are essentially independent of the applied strain: γ_0 = 1.18%, 0.36% and 3.85% for E65, E70, and E74, respectively. For the E samples, in the insets the line shows that the relaxation rate scales as q, indicative of ballistic dynamics. Deviations from ballistic behavior are observed only at very low q, most likely because the decay of g_2-1 is too small for the fit to capture reliably the relaxation time.

II.d Scattering vector dependence of the dynamics and of the model parameters

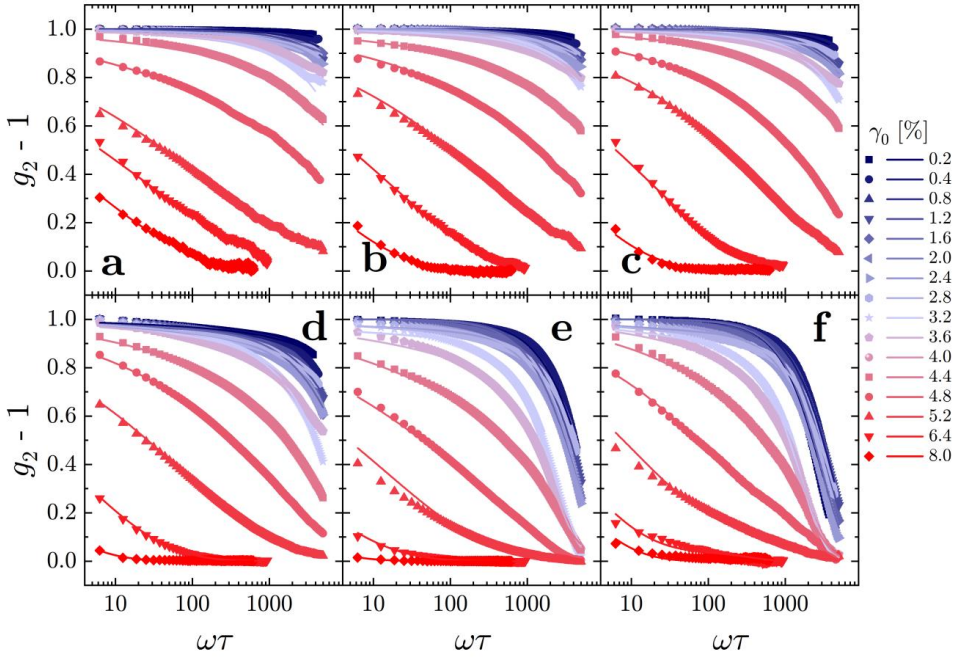

Figure SI6: Scattering vector dependence of correlation functions, sample E64.

Intensity correlation functions for sample E64%, for various imposed strain amplitudes as shown by the labels. Values of the scattering vector q: 0.7 μm^{-1} (a), 1.3 μm^{-1} (b), 2.5 μm^{-1} (c), 4.8 μm^{-1} (d), 9 μm^{-1} (e), 14 μm^{-1} (f).

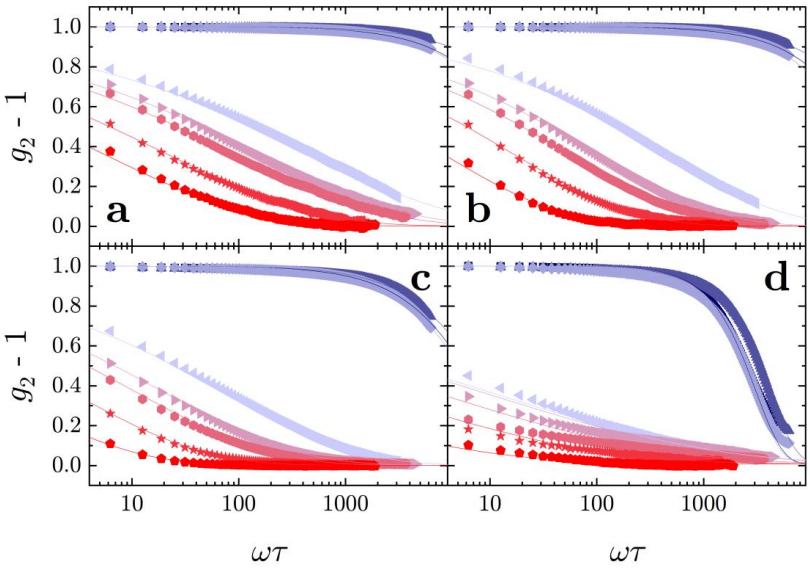

Figure SI7: Scattering vector dependence of correlation functions, sample E74.

Intensity correlation functions for sample E74% (same sample and color code as in Fig. 2c of the main text, which shows data at q = 9 µm^{-1}). Values of the scattering vector q: 1.3 µm^{-1} (a), 2.5 µm^{-1} (b), 4.8 µm^{-1} (c), 14 µm^{-1} (d).

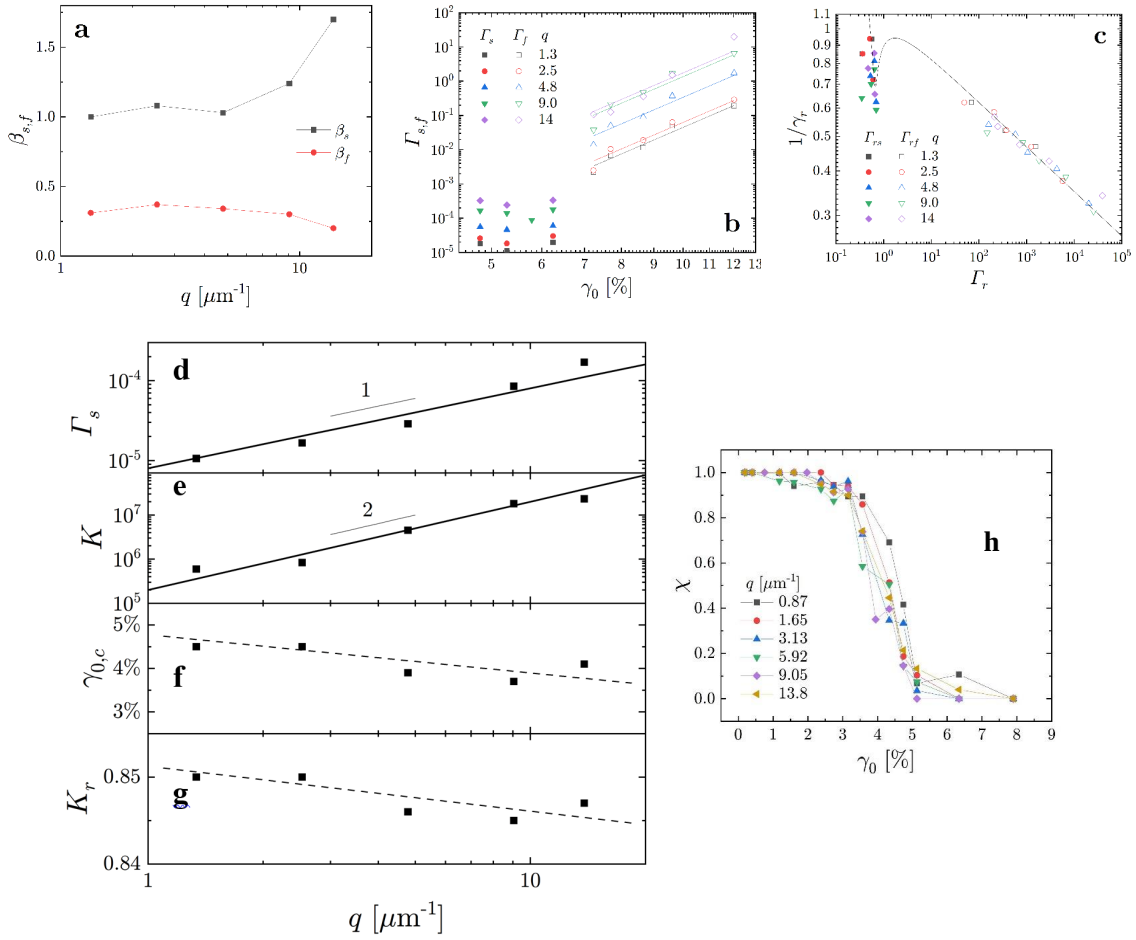

Figure SI8: Scattering vector dependence of various model and fit parameters.

Scattering vector dependence of various model and fit parameters for representative E samples. a-g: sample E74%; h: sample E64%.

a): q dependence of the stretching exponent β_f for the fast decay and compressing exponent β_s for the slow decay. β_f depends only mildly on q. At low q, β_s approaches unity, most likely because the limited decay of g_2-1 prevents the shape of the correlation function to be characterized precisely (see Fig. SI7a-c).

b): q and strain amplitude dependence of the relaxation rates of the fast and slow modes. In the large strain regime, Γ_f grows as a power-law of γ_0, with an exponent n independent of q, as indicated by the parallel lines in the double logarithmic plot.

c): state diagram in the spirit of Fig. 4 of the main text, but obtained from data at different q vectors. All data collapse on the same curve, demonstrating that the model is robust with respect to the choice of q.
d): relaxation rate of the spontaneous dynamics, obtained by extrapolating data under shear to the $\gamma_0 \rightarrow 0$ limit. The relaxation rate increases as q, indicative of ballistic dynamics.
e): the model parameter K (akin to temperature T in Van der Waal's equation of state for real gases) grows as q^2. At large strain, Eqs. 2a-2b of the main text show that $\Gamma \sim \Gamma_f \sim K/\gamma_0^{-n}$. Thus, the $K \sim q^2$ scaling shown here implies $\Gamma \sim \Gamma_f \sim q^2$, i.e. that the dynamics at large strain are diffusive (see also Fig SI9).
f): the yield strain $\gamma_{0,c}$ extracted by fitting the model to the microscopic dynamics exhibits only a mild dependence on the scattering vector q.
g): the model parameter K expressed in reduced units (i.e. K normalized by its value K_c at the critical point) is nearly independent of the q vector.
h): The normalized amplitude of the slow mode, χ, depends only very weakly on the q vector at which the microscopic dynamics are measured. This is consistent with the notion that the yield strain inferred from the microscopic dynamics is nearly insensitive to q, as shown in f. Furthermore, the data in h show that the width of the coexistence region is nearly independent of q. Because in the model the width of the coexistence region is mainly controlled by the amount of disorder, these data indicate that the latter is essentially insensitive to the choice of q.

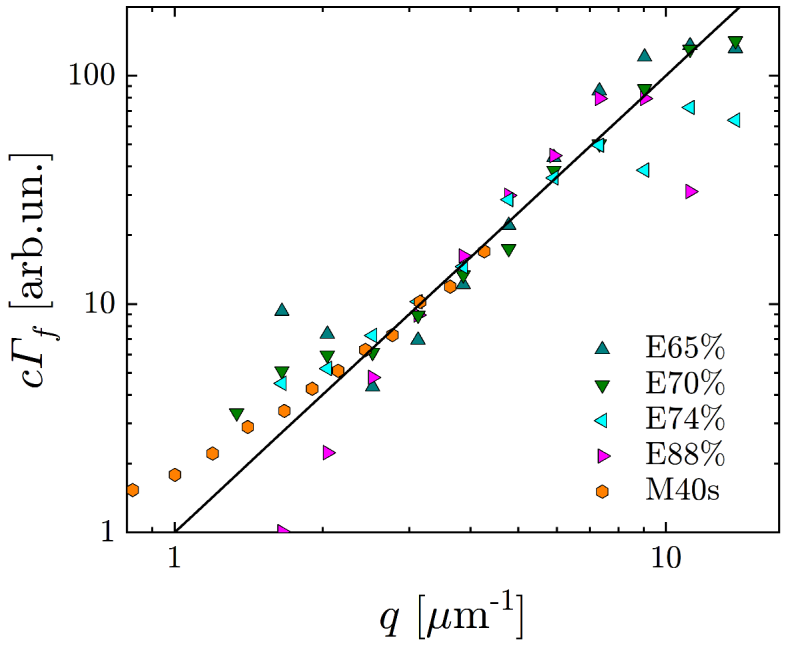

Figure SI9: Diffusive dynamics in the fluidized regime.

Symbols: relaxation rates measured in the fully fluidized regime (strain amplitudes: γ_0=5% for E65% and E70%, γ_0=7% for E74%, γ_0=16% for E88%, γ_0=50% for M40s). Datasets have been rescaled vertically by multiplying them by a constant c, to highlight the overall $\boldsymbol{\Gamma_f \propto q^2}$ behavior indicative of diffusive dynamics (solid line).

II.e Impact of the oscillatory frequency (samples M2s and M40s)

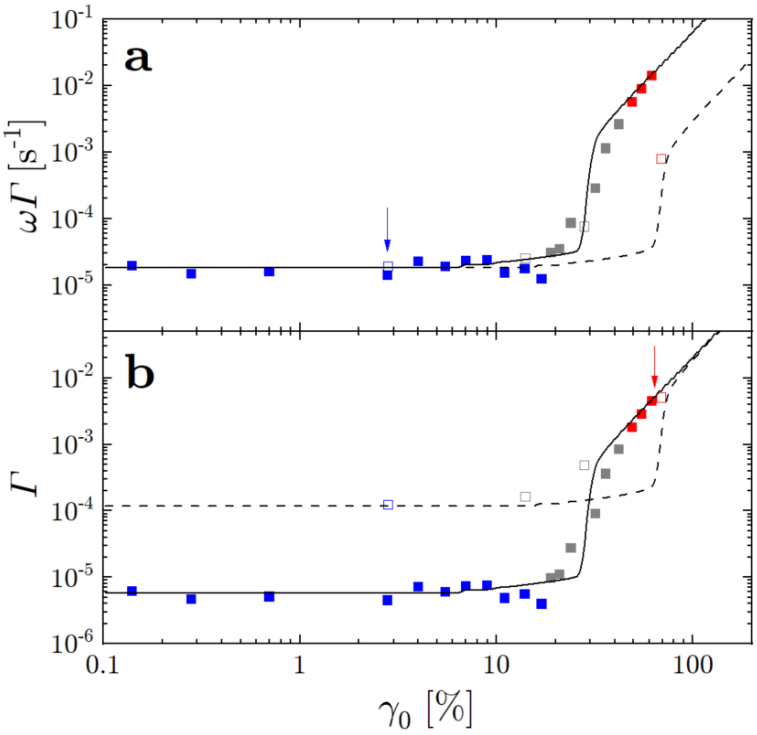

Figure SI10: Impact of oscillatory frequency.

Relaxation rate (a) and normalized relaxation rate (b) as a function of strain amplitude, for dense microgel suspensions measured at two different oscillatory frequencies, corresponding to a period of 2s (full symbols, sample M2s), and 40s (empty symbols, sample M40s), respectively. Blue, red and gray symbols refer to compressed (solid-like), stretched (fluid-like), and two-step (coexistence) relaxations, respectively. Arrows highlight the collapse of solid-like relaxations when using physical units (panel a)), and of liquid-like relaxations when using relaxation rates normalized by the angular frequency of the imposed oscillatory shear (panel b)). Lines: numerical solutions reproducing the observed behavior with shared model parameters $\Gamma_0 = 2\ 10^{-5} s^{-1}$ and $K = 4\ 10^{-3}$. The average coupling constants are $\bar{\bar{\alpha}} = 9\ 10^{-8}$ for M2s (solid line) and $\bar{\alpha} = 1.6\ 10^{-6}$ for M40s (dashed line).

III. NUMERICAL MODEL

	Unit	M2s	M40s	N41%	N41%Aged	N45%	E65%	E70%	E74%	E88%
$1/\tau_0$	1/s	$2\ 10^{-5}$	$2\ 10^{-5}$	10^{-4}	10^{-4}	$1.1\ 10^{-4}$	$1.6\ 10^{-3}$	$1.3\ 10^{-4}$	$6.1\ 10^{-4}$	$6.6\ 10^{-4}$
$1/\omega\tau_0$	-	$6.4\ 10^{-6}$	$1.3\ 10^{-4}$	$3\ 10^{-5}$	$3\ 10^{-5}$	$3.5\ 10^{-5}$	$3\ 10^{-4}$	$2\ 10^{-5}$	10^{-4}	$1.1\ 10^{-4}$
ω	rad/s	3.14	0.157	3.14	3.14	3.14	6.28	6.28	6.28	6.28
$\bar{\alpha}$	-	$9\ 10^{-8}$	$1.6\ 10^{-6}$	$1.4\ 10^{-6}$	$8\ 10^{-3}$	$1.1\ 10^{-3}$	$8.8\ 10^{5}$	$2\ 10^{4}$	$7\ 10^{3}$	$4.9\ 10^{2}$
σ_α^2	-	$8.9\ 10^{-16}$	$1.28\ 10^{-12}$	$4.9\ 10^{-13}$	$3.2\ 10^{-6}$	$9.68\ 10^{-8}$	$2.71\ 10^{11}$	$8\ 10^{5}$	$2.94\ 10^{5}$	48
n	-	3	3	1	3	3	8	8	8	8
K	-	$4\ 10^{-3}$	$4\ 10^{-3}$	$1.3\ 10^{-2}$	62	8	10^{9}	$2.4\ 10^{8}$	$1.8\ 10^{7}$	$1.1\ 10^{6}$
$\omega\Gamma_c$	rad/s	$6\ 10^{-5}$	$6\ 10^{-5}$	$3\ 10^{-4}$	$3\ 10^{-4}$	$3\ 10^{-4}$	$5\ 10^{-3}$	$4\ 10^{-4}$	$1.8\ 10^{-3}$	$2\ 10^{-3}$
Γ_c	-	$1.9\ 10^{-5}$	$4\ 10^{-4}$	$9\ 10^{-5}$	$9\ 10^{-5}$	$1.1\ 10^{-4}$	$8\ 10^{-4}$	$6\ 10^{-6}$	$3\ 10^{-4}$	$3\ 10^{-4}$
K_c	-	$4.2\ 10^{-3}$	$4\ 10^{-3}$	$1.3\ 10^{-2}$	72	9.3	10^{9}	$2.9\ 10^{-3}$	$2.1\ 10^{7}$	$1.4\ 10^{6}$
$\gamma_{0,c}$	-	0.23	0.65	0.027	0.015	0.031	0.035	0.03	0.05	0.07
K_r	-	0.89	0.98	0.97	0.85	0.86	0.99	0.84	0.85	0.84
g	-	0.11	0.02	0.03	0.15	0.14	0.01	0.16	0.15	0.16
d	-	0.11	0.5	0.25	0.05	0.08	0.35	0.002	0.006	0.0002

Table SI2: Model parameters used to reproduce the experiments. The fitting parameters are in **red bold** font, parameters fixed by the experiments are in plain black font, and parameters obtained by combining the formers are in blue font. The fitting parameters are obtained by fitting simultaneously, for each sample, Γ_s, Γ_t, and χ as a function of γ_0, over the whole range of probed strain amplitudes, see e.g. Figs. 2d-2f of the main text.

The parameters listed in the table above have the following meaning:

$1/\tau_0$	Spontaneous relaxation rate (in physical units)
$1/\omega\tau_0$	Normalized spontaneous relaxation rate.
ω	Angular frequency of the imposed oscillatory strain.
$\bar{\alpha}, \sigma_\alpha^2$	Average value and variance of the distribution of coupling constant for the dynamics of neighboring sites.
n	Exponent ruling the strain dependence of the fast mode at large strain amplitude, where $\Gamma_f \sim \gamma_0^n$.
K	Model parameter in Eq. (3) of the main text, analogous to temperature T in Van der Waals' gas equation.
$\omega\Gamma_c$	Relaxation rate (in physical units) at the critical point in the mean field model, see the discussion of Eq. (4) in the main text.
Γ_c	Normalized critical relaxation rate.
K_c	Value of the model parameter K at the critical point in the mean field model, see the discussion of Eq. (4) in the main text.
$\gamma_{0,c}$	Value of the applied strain at the critical point in the mean field model, see the discussion of Eq. (4) in the main text.
K_r	Model parameter K normalized by its critical value: $K_r = K/K_c$.
g	'Glassiness' of a sample, defined by $g = 1 - K_r$
d	Disorder of the coupling constants for the dynamics: $d = \sigma_\alpha^2/\alpha^2$, with σ_α^2 the variance of the distribution of the coupling constants

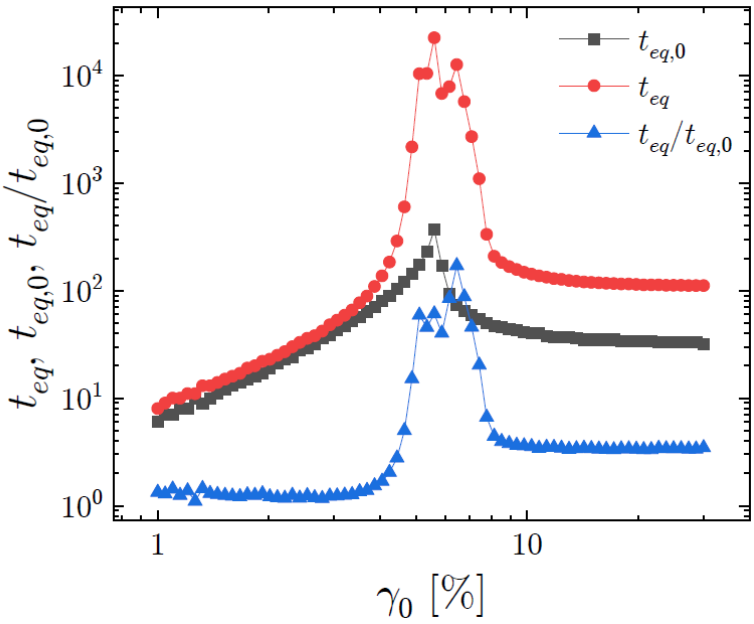

Figure SI11: Convergence of numerical model: equilibration time.

Number of iterations needed for the iterative calculation scheme to converge as a function of the strain amplitude, γ_0, for a model with and without disorder (red circles, t_{eq}, and black squares, $t_{eq,0}$, respectively). Blue triangles: $t_{eq}/ t_{eq,0}$ (also shown in Fig. 5f of the main text). The model is implemented on a 2D lattice with 512 x 512 sites. The model parameters correspond to the fit to sample N45% (see Table SI2).

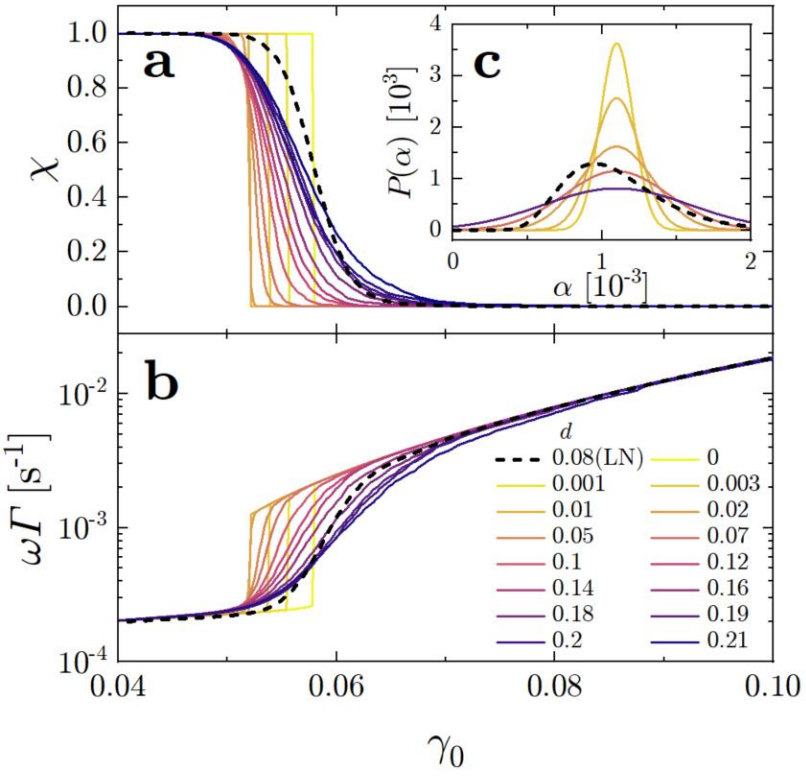

Figure SI12: Dependence on disorder.

Changing the nature of the probability distribution function (PDF) of the coupling constants does not change the main features of the transition. Panels a) and b): Order parameter χ (a) and normalized average relaxation rate Γ (b) extracted from the numerical model as a function of strain amplitude, γ_0, for various PDFs. The model parameters are issued from the fit to N45 (see Table SI2). The coupling constants $\alpha_{i,j}$ are drawn from a Log-Normal PDF (LN, black dashed line), as in the main text, or from Gaussian PDFs, with increasing disorder $d = \sigma_\alpha^2/\bar{\alpha}^2$ from yellow to purple shades, as specified in the legend. The left tails of the Gaussian PDFs are truncated to insure $\alpha_{i,j} \geq 0$. Panel c): representative PDFs used to generate the data in a) and b) (for the sake of clarity, not all the PDFs are shown).

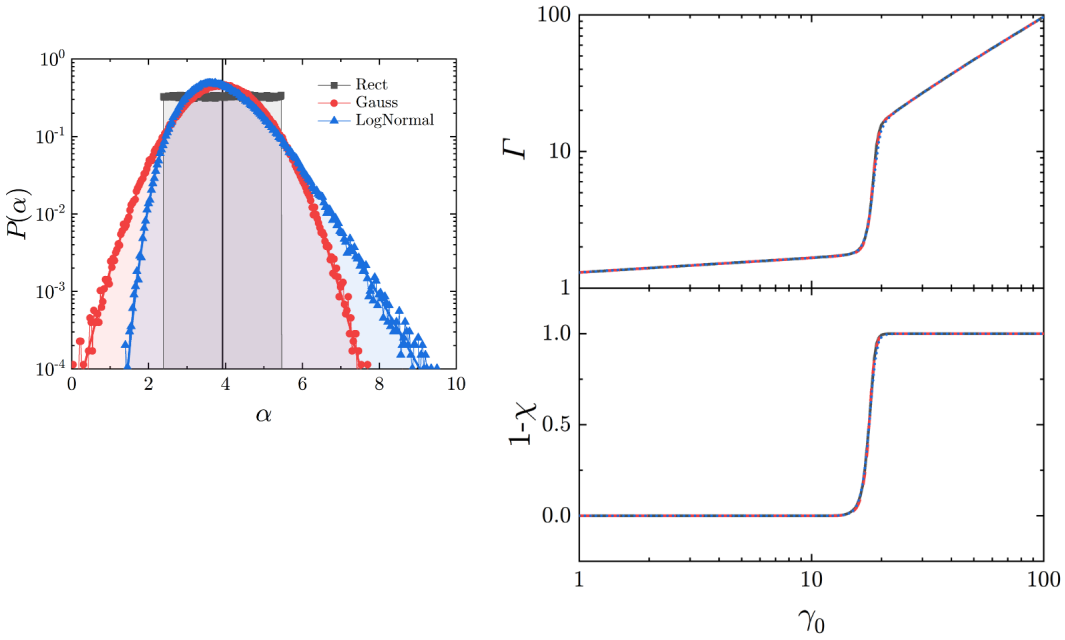

Figure SI13: Changing the PDF of the coupling constants does not modify the model predictions.

Left panel: shape of three probability distribution functions (PDF) used to test numerically the impact of the PDF of the coupling constant α on the predictions of the model. Black, red and blue points refer to a rectangular, Gaussian and log-normal PDF, respectively. The left tail of the Gaussian PDF is truncated to insure $\boldsymbol{\alpha_{i,j} \geq 0}$. The right panels show that the shape of the PDF has no impact on the strain amplitude dependence of the relaxation rate (top) or the relative amplitude of the fast mode χ-1 (bottom).

IV. SPATIAL HETEROGENEITY OF THE DYNAMICS AND SHEAR BANDS

We test in a few samples the spatial heterogeneity of the dynamics and the existence of shear bands.

In the geometry of our experiments, shear bands would develop most likely as layers with different shear deformation organized perpendicularly to the shear gradient direction (the $\overrightarrow{\boldsymbol{u_z}}$ direction in the schemes of Figs. SI1- SI3) and parallel to the shear direction. In the light scattering setups used in this work, the scattered light is collected from the whole thickness of the illuminated sample, with no spatial resolution along the shear gradient direction. It is therefore very difficult to test directly the existence of shear bands. However, we note that if shear bands parallel to the shear direction would exist, the dynamics detected in our space-resolved setup (e.g. the PCI setup of Fig. SI1c) would be spatially homogeneous. Indeed, scattered light exiting from the shear cell and forming the image on the detector would have equally probed all bands, irrespective of the positions in the (x,y) plane that is imaged.

Figure SI14 shows that this is not the case: instead, in the coexistence region the sample partitions in localized domains of fast and slow dynamics, incompatible with shear bands parallel to the shear direction.

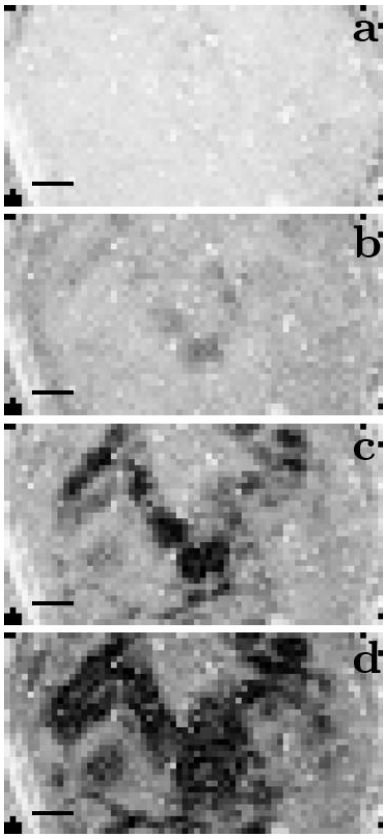

Figure SI14: Coexistence of fast and slow domains as probed by light scattering.

Stroboscopic correlation maps for sample N45% in the coexistence region (strain amplitude γ_0 = 5.7%), for different time delays τ/T = 32 (a), 128 (b), 512 (c), 1024 (d)). The amount of correlation is represented by a gray scale from black (g_2-1=0) to white (g_2-1=1). Scale bars: 1mm.

Experiments on emulsions are consistent with this scenario. They probe a thin sample slab (thickness ~ 0.5 µm, smaller than the drop size), parallel to the shear direction. The observation of the coexistence of two relaxation modes under these conditions (see sample E65%, Fig. SI15) rules out the hypothesis that the

observed bimodal relaxation stems from distinct shear bands organized perpendicularly to the shear gradient direction.

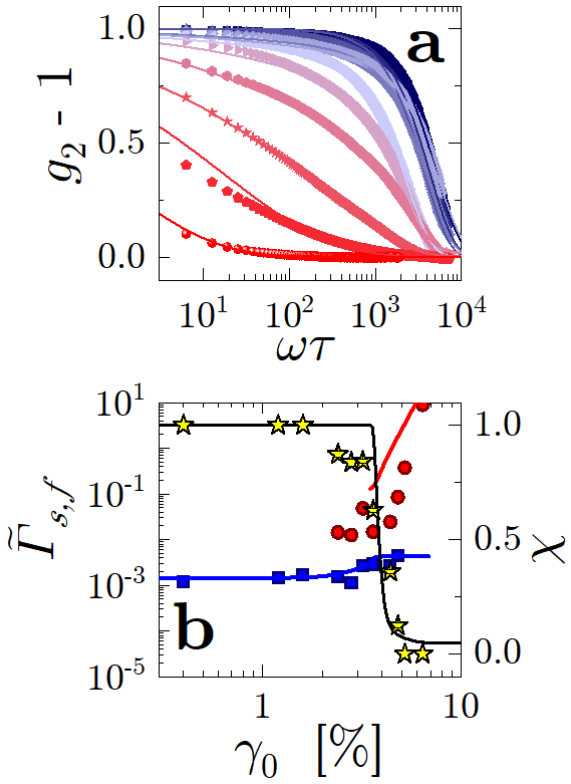

Figure SI15: Dynamic coexistence in emulsions (sample E65%)

a) Intensity correlation functions for sample E65%, plotted *vs* the normalized time delay $\omega\tau$, as in Fig. 2 of the main text. Symbols: experimental data. Lines: fits using Eq. 1 of the main text. b) Symbols: fitting parameters. Left axis: normalized relaxation rates for slow and fast modes (blue squares and red circles, respectively). Right axis: relative amplitude χ of the slow mode (stars). Lines: result of numerical model with parameters reported in Table SI2.

Furthermore, a direct visualization of the regions undergoing fast rearrangements may be obtained by taking the difference between the intensity of microscopy images taken at different times, as shown in Fig. SI16. In this representation, quiescent regions appear uniformly gray, whereas features on the drop size length scale emerge in the rearranged regions. One clearly sees the emergence of localized domains of fast-moving drops, once again incompatible with shear bands parallel to the shear direction.

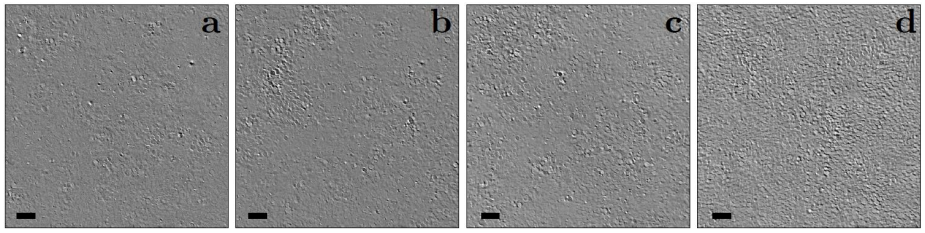

Figure SI16: Coexistence of fast and slow domains as probed by microscopy.

Images obtained by taking the intensity difference between two sample snapshots separated by time delays τ/T = 1 (a), 10 (b), 100 (c), 1000 (d). Data for sample E65%, in the coexistence region (strain amplitude γ_0 = 3.9%). Scale bar: 10 µm.

Finally, in simulations, we find that the system always segregates in mesoscopic domains similar to those shown in Fig. 3c of the main text, with no formation of macroscopic shear bands. An example for various imposed shear amplitudes spanning the coexistence region is shown in Fig. SI17.

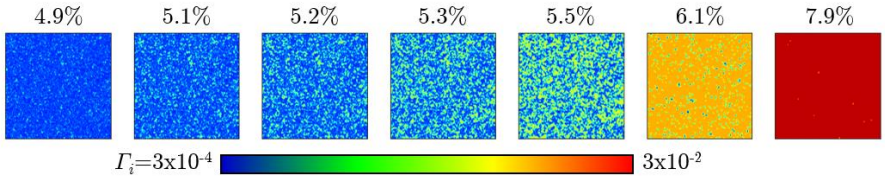

Figure SI17: Coexistence of slow and fast relaxation rates at yielding.

Snapshots of local normalized relaxation rates, Γ_i, at various applied strain amplitudes γ_0 indicated above each panel from lattice simulations. The model parameters are issued from the fit to sample N45% (see Table SI2). Γ_i increases logarithmically from blue to red, as shown by the color bar. Each lattice is composed of 512 x 512 sites, with periodic boundary conditions along both directions.

REFERENCES

[1] B. J. Berne and R. Pecora, *Dynamic Light Scattering: With Applications to Chemistry, Biology, and Physics* (Wiley, 1976).

[2] S. Aime, L. Ramos, J.M. Fromental, G. Prévot, R. Jelinek, and L. Cipelletti, *A stress-controlled shear cell for small-angle light scattering*, Rev. Sci. Instrum. **87**, 123907 (2016)

[3] E. D. Knowlton, private communication.

[4] F. Giavazzi and R. Cerbino, *Digital Fourier Microscopy for Soft Matter Dynamics*, Journal of Optics **16**, 083001 (2014).